

# Spin-2 Resonances in Vector-Boson-Fusion Processes at NLO QCD

Jessica Frank, Michael Rauch, Dieter Zeppenfeld

*Institute for Theoretical Physics, Karlsruhe Institute of Technology, 76128 Karlsruhe, Germany*

## Abstract

The most likely spin assignments of the recently discovered 126 GeV resonance are spin 0 or 2. In order to distinguish the two, we construct an effective Lagrangian model which comprises interactions of a spin-2 electroweak singlet or triplet state with the SM gauge bosons. Within this model, cross sections and differential distributions are calculated and implemented within the Monte Carlo program VBFNLO, which simulates vector-boson-fusion processes at hadron colliders at NLO QCD accuracy. We study the phenomenology of spin-2 resonances produced in vector-boson-fusion processes at the LHC. Specifically, we consider light Higgs-like spin-2 resonances decaying into two photons and show how angular distributions allow us to distinguish between a Standard Model Higgs and a spin-2 resonance. We also investigate the characteristics of heavy spin-2 resonances which decay into two weak gauge bosons, leading to a four-lepton final state.

# 1 Introduction

One of the main tasks of the LHC is to uncover the origin of electroweak symmetry breaking. A giant step in this direction was made recently with the observation of a narrow resonance decaying into pairs of electroweak gauge bosons at an invariant mass of about 126 GeV by the LHC experiments ATLAS [1] and CMS [2]. The data obtained for this resonance, as yet, are compatible with it being a SM Higgs boson [3]. One of the main tasks for the coming years is to perform increasingly stringent tests of the assertion that, indeed, the SM Higgs boson has been found.

There are several possible channels for the detection of the Higgs resonance and for measurements of its properties. A production channel with fairly large cross section is vector-boson-fusion (VBF) [4], which shows a clear signature of two highly energetic jets in the forward and backward regions of the detector. The loop-induced decay to a final state with two photons then allows a full reconstruction of the Higgs' four-momentum, leading to a sharp peak in the di-photon mass spectrum. Thereby, it is possible to distinguish the signal from the large background despite its small branching ratio, and a  $\gamma\gamma$  peak has already been seen in the VBF analysis of CMS [5].

For a definite verification that it is indeed the SM Higgs boson which has been discovered at CERN, all features of the Higgs boson need to be tested [6]. These are its couplings [7] (including its self-couplings [8]), its CP quantum number and its spin [9]. Observation of this resonance in the di-photon channel immediately excludes a spin-1 particle due to the Landau-Yang theorem [10]. Besides the spin-0 of the Higgs boson, a spin-2 particle would also be possible. Since the distinction of a spin-0 and a spin-2 resonance is an important task for Higgs physics, this paper provides tools for differentiating between the two. Specifically, we use an effective Lagrangian for a spin-2 field interacting with electroweak gauge bosons to calculate VBF cross sections and distributions at NLO QCD precision. These calculations are implemented in the VBFNLO program [11], which is then used to search for characteristic differential distributions which distinguish between the two spin choices. Our analysis focuses on angular correlations, since they are known as a powerful tool to study the spin of a resonance.

Due to the high energies which can be achieved with the LHC, it might also be possible to detect some new, heavy resonances in VBF processes, which are manifestations of physics beyond the Standard Model. For these resonances, a spin determination would also be needed. Whereas heavy spin-1 resonances have already been studied within the VBFNLO framework [12], our present analysis will consider the characteristics of heavy spin-2 resonances.

Within the present analysis, the features of spin-2 resonances in VBF are studied for two cases: light, Higgs-like resonances in the photon pair-production channel and heavy resonances in processes with four leptons in the final state (in addition to the two tagging jets characterizing VBF). These are  $e^+ e^- \mu^+ \mu^- jj$ ,  $e^+ e^- \nu_\mu \bar{\nu}_\mu jj$ ,  $e^+ \nu_e \mu^- \bar{\nu}_\mu jj$ ,  $e^+ \nu_e \mu^+ \mu^- jj$  and  $e^- \bar{\nu}_e \mu^+ \mu^- jj$ . Of these, the first one will be studied in most detail, since a final state which does not contain neutrinos allows for a full reconstruction of a resonance. In order to describe the interaction of spin-2 particles with electroweak gauge bosons, we have constructed an effective model which comprises two different scenarios: a

spin-2 state which behaves as a singlet under SU(2) transformations and a spin-2 triplet.

This paper is organized as follows: In Section 2, we present our model for the interaction of neutral and charged spin-2 particles with electroweak bosons. The relevant aspects of our calculation, including our choice of input parameters and selection cuts, are sketched in Section 3. In Section 4 the results of our analysis are presented, where we show the characteristics of spin-2 resonances in the different kinds of processes. Additionally, we discuss to what extent they can be used for a distinction of a spin-2 resonance from a Higgs boson or the SM non-resonant background, respectively. Furthermore, the impact of the NLO QCD corrections is examined. Conclusions are drawn in Section 5. Specific formulas describing the decay widths of the spin-2 particles are given in the Appendix.

## 2 The Spin-2 Model

For the present analysis of spin-2 resonances in vector-boson-fusion processes, we have constructed an effective model describing the interaction of spin-2 particles with electroweak bosons. Two cases are considered: A spin-2 state which behaves as a singlet under SU(2) transformations and a spin-2 state which is a weak isospin triplet.

These states are described by the general spin-2 fields  $T^{\mu\nu}$  (singlet) and  $T_j^{\mu\nu}$  (triplet),

$$T_{(j)}^{\mu\nu}(x) = \int \frac{d^3k}{(2\pi)^3 2k^0} \sum_{\lambda=-2}^2 \left( \varepsilon^{\mu\nu}(k, \lambda) a_{\lambda(j)}(k) e^{-ikx} + \varepsilon^{*\mu\nu}(k, \lambda) a_{\lambda(j)}^\dagger(k) e^{ikx} \right). \quad (2.1)$$

The free Lagrangian for a general spin-2 field with mass  $m$  is given by [13]

$$\mathcal{L}_{\text{free}} = -(\partial_\mu T^{\mu\nu})^\dagger (\partial_\rho T^\rho{}_\nu) + \frac{1}{2} (\partial_\rho T^{\mu\nu})^\dagger (\partial^\rho T_{\mu\nu}) + \frac{m^2}{2} T^{\mu\nu\dagger} T_{\mu\nu}. \quad (2.2)$$

For the triplet field, the partial derivatives are to be replaced by covariant ones in order to account for its gauge couplings to electroweak bosons. Note, however, that these couplings induce  $TTV$  or  $TTVV$  vertices, which do not appear in the processes studied in this paper. The fields are symmetric in  $\mu, \nu$ , transverse and  $T_\mu^\mu = T_\mu^{\mu,j} = 0$ .  $\varepsilon^{\mu\nu}$  is a symmetric polarization tensor built from the usual spin-1 polarization vectors [14]:

$$\begin{aligned} \epsilon^{\mu\nu}(p, \pm 2) &= \epsilon^\mu(p, \pm) \epsilon^\nu(p, \pm) \\ \epsilon^{\mu\nu}(p, \pm 1) &= \frac{1}{\sqrt{2}} (\epsilon^\mu(p, \pm) \epsilon^\nu(p, 0) + \epsilon^\mu(p, 0) \epsilon^\nu(p, \pm)) \\ \epsilon^{\mu\nu}(p, 0) &= \frac{1}{\sqrt{6}} (\epsilon^\mu(p, +) \epsilon^\nu(p, -) + \epsilon^\mu(p, -) \epsilon^\nu(p, +) + 2\epsilon^\mu(p, 0) \epsilon^\nu(p, 0)) . \end{aligned} \quad (2.3)$$

While the spin-2 singlet involves only one uncharged particle, called  $T$ , the triplet consists of three spin-2 particles,  $T^1$ ,  $T^2$  and  $T^3$ , or, equivalently, a charged pair and a neutral particle:

$$\begin{aligned} T^\pm &= \frac{1}{\sqrt{2}} (T^1 \mp i T^2), \\ T^0 &= T^3. \end{aligned} \quad (2.4)$$

Since in the present analysis we only study spin-2 resonances which are produced in electroweak-boson fusion, we restrict ourselves to a model of the interaction of a single spin-2 particle with electroweak bosons. The building blocks of the corresponding singlet and triplet Lagrangian were chosen to be the spin-2 field(s), the vector fields of the electroweak gauge bosons and the scalar Higgs field  $\Phi$ . Respecting gauge and Lorentz invariance and neglecting higher dimensional operators, we end up with the following effective Lagrangian for the singlet case:

$$\mathcal{L}_{\text{singlet}} = \frac{1}{\Lambda} T_{\mu\nu} (f_1 B^{\alpha\nu} B^\mu_\alpha + f_2 W_i^{\alpha\nu} W^{i,\mu}_\alpha + 2f_5 (D^\mu \Phi)^\dagger (D^\nu \Phi)), \quad (2.5)$$

while the Lagrangian corresponding to the triplet case reads

$$\mathcal{L}_{\text{triplet}} = \frac{1}{\Lambda} T_{\mu\nu,j} (f_6 (D^\mu \Phi)^\dagger \sigma^j (D^\nu \Phi) + f_7 W^{j,\mu}_\alpha B^{\alpha\nu}). \quad (2.6)$$

$\Lambda$  is the characteristic energy scale of the underlying new physics,  $f_i$  are variable coupling parameters,  $B^{\alpha\nu}$  and  $W_i^{\alpha\nu}$  are the usual electroweak field strength tensors and  $D^\mu$  is the covariant derivative

$$D^\mu = \partial^\mu - ig W_i^\mu \frac{\sigma^i}{2} - ig' Y B^\mu. \quad (2.7)$$

The terms in Eq. (2.5) and (2.6) exhaust the possible parity-conserving contributions at the dimension five level. The masses of the spin-2 particles are taken as free parameters.

In contrast to the graviton Lagrangian [14], couplings to fermions or gluons are not included in the Lagrangians (2.5, 2.6). Another important difference to the graviton Lagrangian is the presence of variable prefactors  $f_i$ , which are not fixed to the same value by the underlying theory.

It is possible to write down additional terms including the dual electroweak field strength tensors  $\tilde{B}^{\alpha\nu} = \frac{1}{2} \varepsilon^{\alpha\nu\rho\sigma} B_{\rho\sigma}$  and  $\tilde{W}_i^{\alpha\nu}$ , namely  $\frac{f_3}{\Lambda} T_{\mu\nu} \tilde{B}^{\alpha\nu} B^\mu_\alpha$  and  $\frac{f_4}{\Lambda} T_{\mu\nu} \tilde{W}_i^{\alpha\nu} W^{i\mu}_\alpha$ . However, such terms yield  $TVV$  vertices which are proportional to  $T_\mu^\mu$  and, thus, vanish for on-shell spin-2 particles. Off-shell contributions do not lead to significant observable effects in the distributions to be studied below.

The four relevant vertices resulting from the singlet Lagrangian (2.5), which involve two electroweak bosons and the spin-2 particle  $T$ , are  $TW^+W^-$ ,  $TZZ$ ,  $T\gamma\gamma$  and  $T\gamma Z$ . The calculation of the corresponding Feynman rules yields the following expressions for the  $TVV$  vertices:

$$\begin{aligned} TW^+W^- : & \quad \frac{2if_2}{\Lambda} K_1^{\alpha\beta\mu\nu} + \frac{if_5 g^2 v^2}{2\Lambda} K_2^{\alpha\beta\mu\nu}, \\ TZZ : & \quad \frac{2i}{\Lambda} (f_2 c_w^2 + f_1 s_w^2) K_1^{\alpha\beta\mu\nu} + \frac{if_5 v^2}{2\Lambda} (g^2 + g'^2) K_2^{\alpha\beta\mu\nu}, \\ T\gamma\gamma : & \quad \frac{2i}{\Lambda} (f_1 c_w^2 + f_2 s_w^2) K_1^{\alpha\beta\mu\nu}, \\ T\gamma Z : & \quad \frac{2i}{\Lambda} c_w s_w (f_2 - f_1) K_1^{\alpha\beta\mu\nu}, \end{aligned} \quad (2.8)$$

where  $c_w$  and  $s_w$  denote the cosine and sine of the Weinberg angle,  $v$  is the vacuum expectation value of the Higgs field and the two different tensor structures are given by

$$\begin{aligned} K_1^{\alpha\beta\mu\nu} &= p_1^\nu p_2^\mu g^{\alpha\beta} - p_1^\beta p_2^\nu g^{\alpha\mu} - p_2^\alpha p_1^\nu g^{\beta\mu} + p_1 \cdot p_2 g^{\alpha\nu} g^{\beta\mu}, \\ K_2^{\alpha\beta\mu\nu} &= g^{\alpha\nu} g^{\beta\mu}. \end{aligned} \quad (2.9)$$

The indices  $\mu$  and  $\nu$  correspond to the spin-2 field (which is symmetric),  $\alpha$  is the index of the first electroweak boson, whose incoming four-momentum is denoted as  $p_1$ , and  $\beta$  is the index of the second one with four-momentum  $p_2$ .

The triplet Lagrangian (2.6) yields the same relevant vertices for the uncharged spin-2 particle  $T^0$  as the singlet Lagrangian and two additional relevant vertices for the charged particles  $T^+$  and  $T^-$ . The structure of the Feynman rules is analogous to the singlet case:

$$\begin{aligned} T^0 W^+ W^- &: \frac{if_6}{4\Lambda} g^2 v^2 K_2^{\alpha\beta\mu\nu}, \\ T^0 Z Z &: -\frac{if_6}{4\Lambda} (g^2 + g'^2) v^2 K_2^{\alpha\beta\mu\nu} - \frac{2if_7}{\Lambda} c_w s_w K_1^{\alpha\beta\mu\nu}, \\ T^0 \gamma \gamma &: \frac{2if_7}{\Lambda} c_w s_w K_1^{\alpha\beta\mu\nu}, \\ T^0 \gamma Z &: \frac{if_7}{\Lambda} (c_w^2 - s_w^2) K_1^{\alpha\beta\mu\nu}, \\ T^\pm W^\mp Z &: -\frac{if_6}{4\Lambda} g v^2 \sqrt{g^2 + g'^2} K_2^{\alpha\beta\mu\nu} - \frac{if_7}{\Lambda} s_w K_1^{\alpha\beta\mu\nu}, \\ T^\pm W^\mp \gamma &: \frac{if_7}{\Lambda} c_w K_1^{\alpha\beta\mu\nu}, \end{aligned} \quad (2.10)$$

with  $K_1^{\alpha\beta\mu\nu}$  and  $K_2^{\alpha\beta\mu\nu}$  defined as in the singlet case (Eq. (2.9)).

The propagator of the spin-2 field with momentum  $k$ , i.e. the Fourier transform of  $\langle 0 | \mathcal{T} (T^{\mu\nu}(x) T^{\alpha\beta}(0)) | 0 \rangle$ , is given by [14, 15]

$$\frac{i B^{\mu\nu\alpha\beta}(k)}{k^2 - m_T^2 + i m_T \Gamma_T}, \quad (2.11)$$

where  $m_T$  is the mass of the spin-2 particle,  $\Gamma_T$  is its width and  $B^{\mu\nu\alpha\beta}(k)$  is defined as

$$\begin{aligned} B^{\mu\nu\alpha\beta}(k) &= \frac{1}{2} (g^{\mu\alpha} g^{\nu\beta} + g^{\mu\beta} g^{\nu\alpha} - g^{\mu\nu} g^{\alpha\beta}) + \frac{1}{6} \left( g^{\mu\nu} + \frac{2}{m_T^2} k^\mu k^\nu \right) \left( g^{\alpha\beta} + \frac{2}{m_T^2} k^\alpha k^\beta \right) \\ &\quad - \frac{1}{2m_T^2} (g^{\mu\alpha} k^\nu k^\beta + g^{\nu\beta} k^\mu k^\alpha + g^{\mu\beta} k^\nu k^\alpha + g^{\nu\alpha} k^\mu k^\beta). \end{aligned} \quad (2.12)$$

Explicit expressions for the partial decay widths into all possible final states are given in App. A.

Since the present spin-2 model is based on an effective Lagrangian approach, it violates unitarity above a certain energy scale. In order to parametrize high-energy contributions

beyond this effective model, we introduce the following formfactor, which can be multiplied with the amplitudes:

$$f(p_1^2, p_2^2, k_{\text{sp}2}^2) = \left( \frac{\Lambda_{ff}^2}{|p_1^2| + \Lambda_{ff}^2} \cdot \frac{\Lambda_{ff}^2}{|p_2^2| + \Lambda_{ff}^2} \cdot \frac{\Lambda_{ff}^2}{|k_{\text{sp}2}^2| + \Lambda_{ff}^2} \right)^{n_{ff}}, \quad (2.13)$$

where  $p_1^2$  and  $p_2^2$  are the invariant masses of the initial electroweak bosons and  $k_{\text{sp}2}^2$  is the squared invariant mass of the sum of the initial boson momenta, equivalent to that of an  $s$ -channel spin-2 particle. The energy scale  $\Lambda_{ff}$  and the exponent  $n_{ff}$  are free parameters, describing the scale of the cutoff and the suppression power, respectively.

### 3 Elements of the Calculation

For the present analysis, we use the parton-level Monte Carlo program VBFNLO [11], which simulates vector-boson-fusion processes at hadron colliders with NLO QCD accuracy. The characteristics of spin-2 resonances are studied for two different classes of processes: VBF photon pair-production in association with two jets and processes with four leptons and two jets in the final states, namely  $e^+ e^- \mu^+ \mu^- jj$ ,  $e^+ e^- \nu_\mu \bar{\nu}_\mu jj$ ,  $e^+ \nu_e \mu^- \bar{\nu}_\mu jj$ ,  $e^+ \nu_e \mu^+ \mu^- jj$  and  $e^- \bar{\nu}_e \mu^+ \mu^- jj$  production.

The VBF processes with four leptons and two jets in the final state have already been analyzed at NLO QCD accuracy within the SM. These calculations, which are described in Refs. [16], [17] and [18], have been extended by the effects of the spin-2 model for the present analysis. Both resonant and non-resonant sub-processes in typical VBF phase-space regions are considered. The contributing Feynman graphs at tree-level can be grouped into different topologies, where either one, two or three electroweak bosons are attached to the same quark line. Quark–anti-quark initiated  $t$ -channel processes, resulting from crossing the respective quark-quark diagrams, and  $u$ -channel diagrams obtained by interchanging identical initial- or final-state quarks, are also fully taken into account. However, interference between  $t$ - and  $u$ -channel contributions can safely be neglected in VBF phase-space regions.  $s$ -channel exchange, which corresponds to triple vector-boson production, with one of the time-like bosons decaying into a pair of jets, is considered as a separate process in VBFNLO which, however, is strongly suppressed in VBF phase-space regions and will not be considered in the following.

The only tree-level topology in which the spin-2 particles of our model can be exchanged is shown in Fig. 1.

The circular area of Fig. 1 comprises various SM and BSM sub-diagrams which are added, with the result being described by leptonic tensors. Since these tensors are independent of the QCD part, in particular since they do not affect the structure of NLO QCD corrections, they can be modified to include arbitrary new physics effects and then immediately yield cross sections at NLO QCD accuracy: In addition to potential modifications of Higgs contributions, one needs to extend the SM leptonic tensors by the additional Feynman graphs involving spin-2 particles.

For  $VV \rightarrow e^+ e^- \mu^+ \mu^-$ , the electroweak sub-process of  $pp \rightarrow e^+ e^- \mu^+ \mu^- jj$ , these additional diagrams are depicted in Figs. 2 and 3, respectively. Fig. 2 shows the graphs

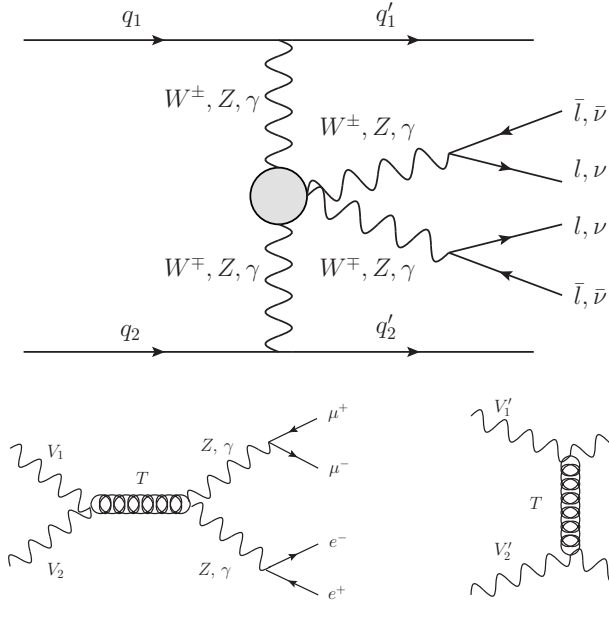


Figure 1: General vector-boson-fusion Feynman graph at tree-level, where spin-2 effects can appear.

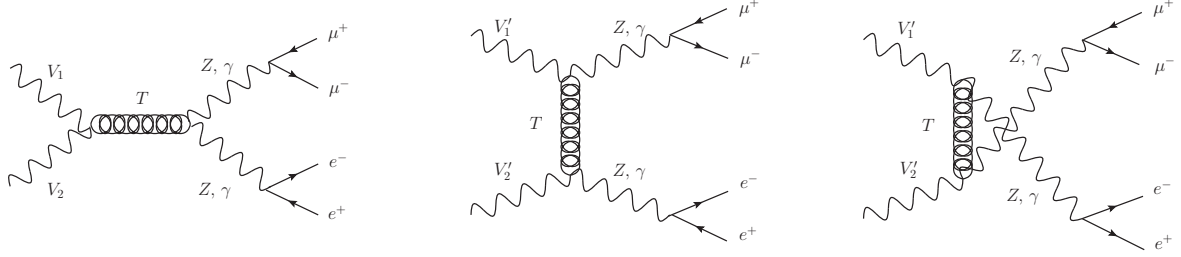


Figure 2: Feynman graphs of the sub-process  $VV \rightarrow e^+ e^- \mu^+ \mu^-$  involving the spin-2 singlet particle  $T$ , with  $V_1 V_2 \cong W^+ W^-, \gamma Z, Z\gamma, \gamma\gamma, ZZ$  and  $V_1' V_2' \cong \gamma Z, Z\gamma, \gamma\gamma, ZZ$ .

involving the spin-2 singlet particle  $T$ . The diagrams for the neutral spin-2 triplet are the same as for the singlet particle, with  $T^0$  instead of  $T$ . The Feynman graphs for contributions of charged triplet particles are depicted in Fig. 3.

For the other processes with four leptons and two jets in the final state, the additional Feynman diagrams are analogous and can be found in Ref. [19].

Within the VBFNLO program, the leptonic tensors for a given process do not change when going from LO to NLO contributions, nor do they change between quark and anti-quark initiated sub-processes. Thus they are calculated once per phase-space point and reused, which considerably speeds up the program. The Feynman diagrams contributing to the leptonic tensors are calculated via calls of HELAS routines [20]. For the calculation of the graphs involving spin-2 particles, we created new HELAS routines containing the Feynman rules of the spin-2 model and also a (faster) code which directly determines the spin-2 resonance contributions to the leptonic tensors.

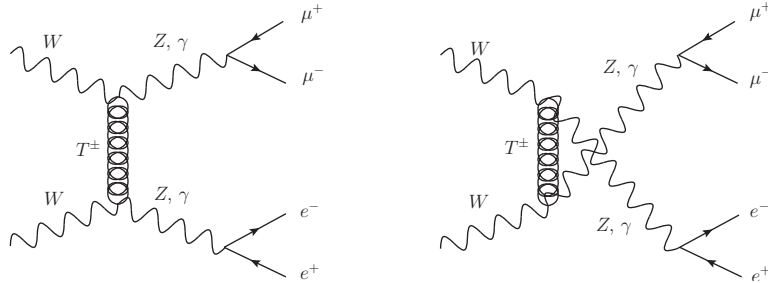


Figure 3: Feynman graphs of the sub-process  $VV \rightarrow e^+ e^- \mu^+ \mu^-$  involving charged spin-2 triplet particles.

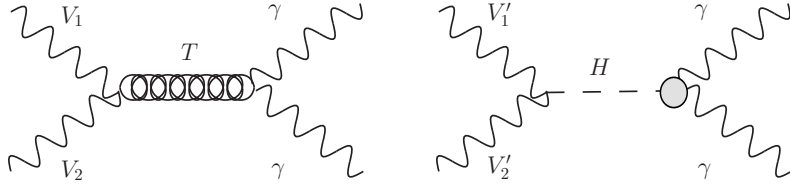


Figure 4: Feynman graphs of the sub-process  $VV \rightarrow \gamma\gamma$ . Left hand side: via a spin-2 resonance (singlet or neutral triplet), with  $V_1 V_2 \triangleq W^+ W^-, \gamma Z, Z\gamma, \gamma\gamma, ZZ$ . Right hand side: via a Higgs resonance, with  $V'_1 V'_2 \triangleq W^+ W^-, ZZ$ .

In the analysis of spin-2 resonances in the VBF process  $qq \rightarrow qq\gamma\gamma$ , we only consider sub-diagrams with resonant production of spin-2 particles, which are shown on the left hand side of Fig. 4. Here,  $T$  denotes either the singlet or the neutral triplet particle. The SM continuum contributions are omitted, because interference effects with the spin-2 resonance are small for a narrow resonance. Thus, the continuum background can be eliminated via a sideband analysis, similar to the SM Higgs case (see Sec. 4.1). We have analyzed the non-resonant spin-2 contributions as well, yet they were found to yield no significant modifications. The characteristics of light spin-2 resonances in this process are compared to those of a SM Higgs resonance. For the analysis of the latter case, we only consider analogous sub-diagrams with an effective  $H\gamma\gamma$  coupling [21], which are depicted on the right hand side of Fig. 4. The results have been cross-checked with another existing implementation of VBF Higgs + 2 jet production, with the Higgs boson decaying into two photons in the narrow-width approximation [11, 22].

Since the spin-2 model only affects the electroweak part of the VBF processes, the NLO QCD corrections are similar to those of the SM and can be adapted from the respective calculations, which are described in detail in Refs. [16] and [22]. The real-emission contributions are obtained by attaching an external gluon to the two quarks lines of Fig. 1 in all possible ways, which also comprises quark-gluon initiated sub-processes. Due to the color-singlet structure of VBF processes, the virtual corrections only comprise Feynman diagrams with a virtual gluon attached to a single quark line. Since the processes with four leptons and two jets in the final state contain graphs with three electroweak bosons attached to a quark line, they contain at most pentagon contributions to the virtual corrections. The other graphs give rise to box, vertex and quark self-energy corrections. In the photon pair-production process, where we only consider graphs with a single electroweak boson attached to a quark line, the virtual corrections are much simpler, since there are no box and pentagon contributions. Representative diagrams for the real emission and the virtual corrections are depicted in Fig. 5.

In the calculation of the NLO corrections, infrared singularities arise both from virtual corrections and from soft and collinear phase-space regions in the real emission part. They are canceled against each other by using the Catani-Seymour dipole subtraction method [23]. The regularization is performed in the dimensional-reduction scheme in  $d = 4 - 2\epsilon$  dimensions [24]. For the evaluation of the finite parts of the virtual corrections, the Denner–Dittmaier scheme [25] is applied for five-point functions and the Passarino–Veltman reduction formalism [26] for loop functions up to four external legs.

Throughout the calculation, the Cabibbo–Kobayashi–Maskawa matrix  $V_{\text{CKM}}$  is ap-



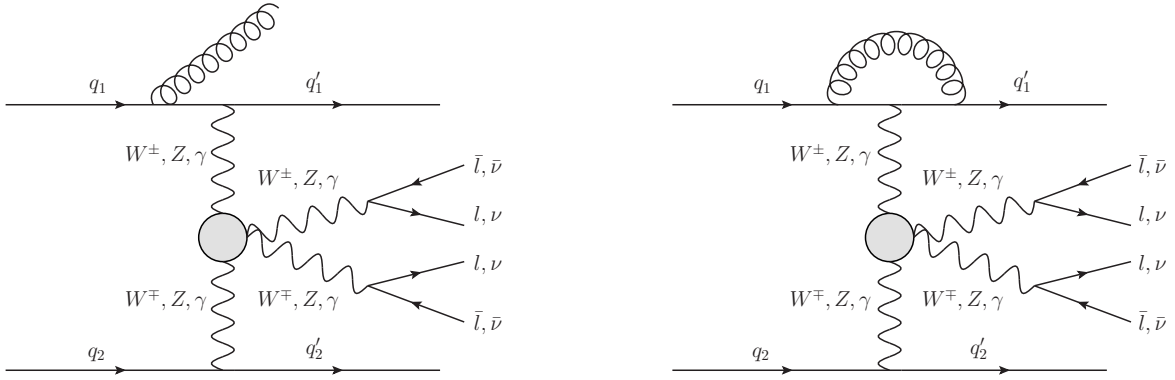


Figure 5: Representative vector-boson-fusion Feynman graphs at NLO QCD. Left hand side: real emission, right hand side: virtual correction.

proximated by the identity matrix. This gives the same results as the exact matrix  $V_{\text{CKM}}$  for the sum over all quark flavors (as long as no final-state flavor tagging is done and mixing with the massive top quark is neglected), since  $V_{\text{CKM}}$  is unitary.

Finite-width effects in massive vector-boson propagators are taken into account by using a modified version [21, 27] of the complex-mass scheme [28], where  $m_V^2$  is replaced with  $m_V^2 - im_V\Gamma_V$ , while a real value for  $\sin^2\theta_W$  is kept. This replacement includes the  $m_V^2$  appearing in the spin part of the propagator in the unitary gauge. This approach is analogous to the one implemented in MadGraph [21] and, indeed, our SM amplitudes agree with the ones obtained with MadGraph.

In the full complex-mass scheme the SM amplitudes are gauge invariant. The BSM contributions appear as  $s$ -,  $t$ - and/or  $u$ - channel spin-2 exchange graphs in weak-boson scattering with a single spin-2 propagator. Since they are derived from the gauge invariant Lagrangians (2.5) or (2.6), the resulting amplitudes are gauge invariant in the absence of finite-width effects. One might worry that using the finite-width propagator (2.11) for the spin-2 fields might break electroweak gauge invariance. We have checked, however, that changing to the overall-factor scheme (which respects gauge invariance), i.e. removing the width from all spin-2 propagators and multiplying the total BSM amplitude with a factor  $\frac{(p^2-m^2)}{(p^2-m^2+im\Gamma)}$ , leaves our results unchanged within the numerical accuracy. Here  $p$ ,  $m$  and  $\Gamma$  denote the momentum, mass and width of the  $s$ -channel spin-2 particle, respectively. While our approach to the handling of finite-width effects is not fully gauge invariant, a comparison with fully gauge invariant amplitudes shows that this does not lead to noticeable deviations at LHC energies.<sup>1</sup>

### 3.1 Input parameters and selection cuts

As electroweak input parameters, we choose  $m_W = 80.399$  GeV,  $m_Z = 91.1876$  GeV and  $G_F = 1.16637 \cdot 10^{-5}$  GeV<sup>-2</sup>, which are taken from the 2010 results of the Particle Data Group [29].  $\alpha$  and  $\sin^2\theta_W$  are derived from these quantities using tree-level electroweak re-

<sup>1</sup>For processes which include graphs with two or more spin-2 particles, the propagator of Eq. (2.11) would require further modification to insure gauge invariance. This complication does not arise in the present context.

lations. We use the CTEQ6L1 [30] parton distribution functions at LO and the CT10 [31] set at NLO with  $\alpha_s(m_Z) = 0.118$ . The factorization scale and the renormalization scale are set to  $\mu_F = \mu_R = Q = \sqrt{|q_{if}^2|}$ , where  $q_{if}$  is the 4-momentum transfer between the respective initial and final state quarks. With this scale choice, LO calculations were found to give a good approximation of NLO cross sections and distributions, while the NLO results are hardly sensitive to the scale choice [18]. Jets are recombined from the final state partons by using the  $k_\perp$  jet finding algorithm [32].

Vector-boson-fusion events are characterized by two tagging jets in the forward regions, with decay products of the vector bosons lying in the central-rapidity region between them. By applying the following inclusive VBF cuts, these features can be used to improve the signal-to-background ratio. The two tagging jets (i.e. the two jets of highest transverse momentum) are supposed to lie inside the rapidity range accessible to the detector and to have large transverse momenta:

$$p_{T,j}^{\text{tag}} > 30 \text{ GeV}, \quad |\eta_j| < 4.5. \quad (3.1)$$

They are reconstructed from massless partons of pseudorapidity  $|\eta| < 5$  and have to be well separated:

$$\Delta R_{jj} \equiv \sqrt{(\eta_{j1} - \eta_{j2})^2 + (\phi_{j1} - \phi_{j2})^2} > 0.7. \quad (3.2)$$

In order to reduce backgrounds and make use of the characteristic features of the VBF channel, we require a large rapidity separation of the tagging jets

$$\Delta\eta_{jj} > 4, \quad (3.3)$$

which have to be located in opposite detector hemispheres,

$$\eta_{j1}^{\text{tag}} \times \eta_{j2}^{\text{tag}} < 0 \quad (3.4)$$

and have a large invariant mass

$$m_{jj} > m_{jj}^{\text{min}}, \quad (3.5)$$

where  $m_{jj}^{\text{min}} = 1000 \text{ GeV}$  for the process  $pp \rightarrow e^+ \nu_e \mu^- \bar{\nu}_\mu jj$  (i.e. “ $W^+W^-jj$  production”) and  $m_{jj}^{\text{min}} = 500 \text{ GeV}$  for all other processes considered in the present analysis.

The charged decay leptons (or decay photons, respectively) are required to be hard, located at central rapidities and well-separated from the jets:

$$p_{T,l} > 20 \text{ GeV}, \quad |\eta_l| < 2.5, \quad \Delta R_{lj} > 0.4. \quad (3.6)$$

Furthermore, they are supposed to fall into the rapidity gap between the two tagging jets:

$$\eta_{j,\text{min}}^{\text{tag}} < \eta_l < \eta_{j,\text{max}}^{\text{tag}}. \quad (3.7)$$

Here,  $l$  denotes a charged lepton or a photon, depending on the considered process. In order to have isolated photons, we require an additional minimal photon-photon  $R$ -separation

$$\Delta R_{\gamma\gamma} > 0.4 \quad (3.8)$$

and impose photon isolation from hadronic activity as suggested in Ref. [33] with separation parameter  $\delta_0 = 0.7$ , efficiency  $\epsilon = 1$  and exponent  $n = 1$ .

To avoid singularities from quasi-collinear  $\gamma^* \rightarrow l^+ l^-$  decays, we apply a cut on the invariant mass of two same-flavor charged leptons,

$$m_{ll} > 15 \text{ GeV}. \quad (3.9)$$

By imposing this set of cuts, the LO differential cross sections are finite, since they lead to finite scattering angles for the two jets. In the NLO calculation, initial state singularities arise, resulting from collinear quark and gluon splittings ( $q \rightarrow qg$  and  $g \rightarrow q\bar{q}$ ). They are factorized into the PDFs. Moreover, divergences from  $t$ -channel exchange of photons with low virtuality appear in the real-emission part, when the additional parton radiation is resolved as a separate jet, but for the other, non-radiating, quark line the initial- and final-state quarks become collinear. These divergences are of electroweak origin and could be removed by including a photon density in the proton PDFs. However, the precise treatment of these divergences does not appreciably affect the cross section, in particular when VBF cuts are applied [27]. Therefore, we eliminate them by imposing an additional cut on the photon virtuality,

$$Q_\gamma^2 > 4 \text{ GeV}^2. \quad (3.10)$$

When distributions of a spin-2 resonance in the processes with four leptons and two jets in the final state are studied, it is convenient to cut off contributions which do not stem from the resonance. Therefore, a minimal and a maximal invariant mass of the final-state lepton system can be required. Whenever such a cut is applied, it will be specified in the corresponding section.

## 4 Results

### 4.1 VBF photon pair-production via Higgs or Spin-2 resonances

In this section, we present numerical results of our analysis of Higgs and spin-2 resonances in VBF photon pair-production in association with two jets. We list the cross sections at LO and NLO QCD accuracy, discuss transverse-momentum distributions and the relevance of the formfactor (2.13) and present angular distributions. Thereby, we investigate whether a spin-2 and a SM Higgs resonance can be distinguished from one another. Additionally, different parameter settings of the spin-2 model are studied and the spin-2 singlet is compared to the spin-2 triplet case. Furthermore, the impact of the NLO QCD corrections is analyzed.

If not indicated otherwise, we consider a spin-2 singlet resonance with couplings  $f_1 = 0.04$ ,  $f_2 = 0.08$ ,  $f_5 = 10$ ,  $f_{i \neq 1,2,5} = 0$  and  $\Lambda = 21 \text{ TeV}$ . The parameters of the formfactor are  $\Lambda_{ff} = 400 \text{ GeV}$ ,  $n_{ff} = 3$ . These parameters are chosen in order to approximately reproduce the relative branching ratios for a SM Higgs boson of mass  $126 \text{ GeV}$  decaying into  $\gamma\gamma$ ,  $WW$  and  $ZZ$  as well as the SM predictions for the transverse momentum distributions of the tagging jets in VBF Higgs boson production at the LHC (see below).

$\sqrt{S}$	LO cross section [fb]		NLO cross section [fb]		$K = \frac{\sigma_{\text{NLO}}}{\sigma_{\text{LO}}}$	
	8 TeV	14 TeV	8 TeV	14 TeV	8 TeV	14 TeV
Higgs	0.7348(3)	2.179(1)	0.7448(4)	2.241(1)	1.014	1.028
Spin-2 singlet	0.7711(4)	2.409(1)	0.7878(4)	2.495(1)	1.022	1.036
Spin-2 triplet	0.7927(4)	1.969(1)	0.8041(5)	2.098(1)	1.014	1.066

Table 1: Integrated cross sections for different types of resonances at LO and NLO QCD accuracy for VBF photon pair-production. The cuts of Section 3.1 are applied.

For the triplet case, we use the same parameters for the formfactor settings, but set the couplings to  $f_6 = f_7 = 1$ ,  $f_{i \neq 6,7} = 0$ ,  $\Lambda = 9$  TeV. The mass of the Higgs boson and the spin-2 particles is set to 126 GeV and we assume  $pp$  collisions at a centre of mass energy of 8 TeV. In the following, when figures compare different values of coupling parameters, couplings  $f_i$  which are not given explicitly are set to zero and  $\Lambda$  is adjusted such that the cross section is approximately the same as the one of the SM Higgs resonance. If not indicated otherwise, differential distributions are determined in the laboratory frame.

In order to analyze possible effects of a finite detector resolution, a smearing of the energy and the transverse momenta of the final-state photons and jets according to a Gaussian distribution was performed, which is based on a CMS Monte-Carlo study [34]. However, this smearing was found to have no significant influence on the distributions we studied. Therefore, the results which are presented here were performed without smearing.

Table 1 gives a comparison of the integrated cross sections for Higgs and spin-2 resonances in the photon pair-production process at LO and NLO QCD accuracy. Numbers are shown for the LHC at a centre of mass energy of 8 TeV as well as for 14 TeV. The shape of the distributions, which we will show in the next part, is identical in both cases, so we will restrict ourselves to the 8 TeV case there. The  $K$ -factor is defined as  $K = \sigma_{\text{NLO}}/\sigma_{\text{LO}}$ . The statistical errors from the Monte Carlo integration are around one per mill for all the different parameter settings we study in this section. Due to the scale choice  $\mu_F = \mu_R = Q$  (see Sec. 3.1), the NLO corrections are quite small. They are roughly the same for a Higgs and a spin-2 resonance.

The width of the Higgs resonance is only  $\approx 4$  MeV, whereas the width of the spin-2 resonance is even much smaller for all the different parameter settings studied here and does not exceed 0.05 MeV (see App. A for details). In principle, the width of the spin-2 resonance can be adjusted to the one of the Higgs by choosing a smaller value of the branching ratio parameter  $b$ , which quantifies the amount of additional, possibly hard to detect, decay modes of the spin-2 particle, such as  $T \rightarrow gg$  which could be induced by a effective  $Tgg$  coupling analogous to the  $f_1$  and  $f_2$  terms in Eq. (2.5). At the same time,  $\Lambda$  can be tuned such that the cross section remains comparable to the Higgs case. However, the width of the resonance peak in the di-photon mass spectrum is dominated by the experimental resolution, which is about a GeV for CMS and ATLAS. Therefore, these details do not play any role.

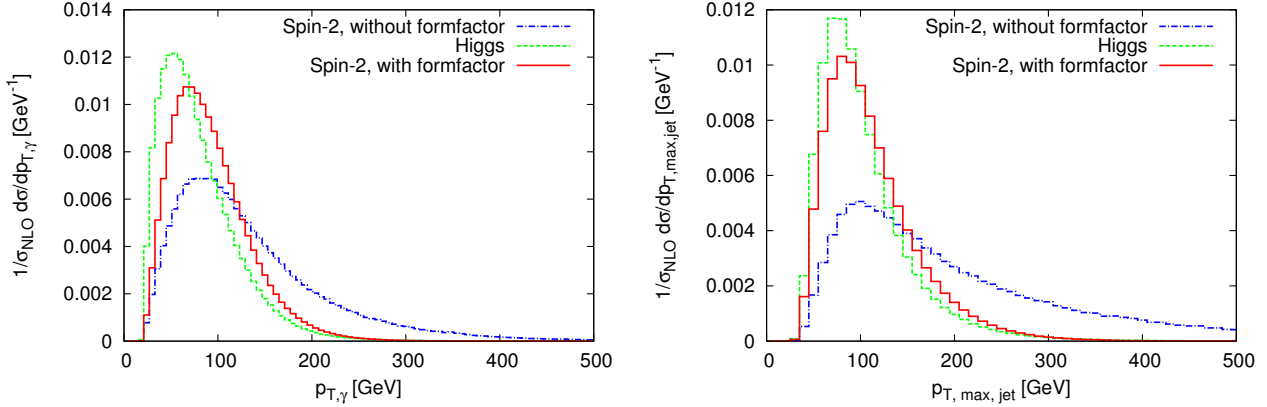


Figure 6: Transverse-momentum distributions for a Higgs and for a spin-2 resonance with couplings  $f_1 = 0.04$ ,  $f_2 = 0.08$ ,  $f_5 = 10$ ,  $f_{i \neq 1,2,5} = 0$ , with and without formfactor, at NLO QCD accuracy. Left hand side:  $p_T$  of a final-state photon, right hand side:  $p_T$  of the tagging jet with the largest transverse momentum.

#### 4.1.1 Transverse-momentum distributions and formfactor

Fig. 6 depicts the normalized transverse-momentum distributions of a final-state photon and of the tagging jet with the largest transverse momentum for a Higgs and a spin-2 singlet resonance with and without the formfactor (2.13) at NLO QCD accuracy. For a spin-2 resonance without the formfactor (or with  $n_{ff} = 0$  or  $\Lambda_{ff} \rightarrow \infty$ , respectively), the transverse momenta of the photons and the hardest jet are much higher than for a Higgs, so that both cases could be easily distinguished from one another via the  $p_T$  distributions. However, the harder  $p_T$  distributions for the spin-2 case are mainly due to the higher energy dimensions of the couplings in the effective Lagrangians (2.5) and (2.6) rather than being a measure of the spin of the resonance. Furthermore, unitarity of the S-matrix in elastic weak-boson scattering is violated for the present spin-2 model if no formfactor is applied (for more details, see Ref. [19]). By a judicious choice of the formfactors, e.g. Eq. (2.13) with  $\Lambda_{ff} = 400$  GeV,  $n_{ff} = 3$ , the  $p_T$  distributions of the spin-2 resonance can be adjusted to closely resemble those of the SM Higgs boson. This works for the transverse momenta of the photons and the jets simultaneously (see Fig. 6). Therefore, transverse-momentum distributions which look like those of the Higgs would not be a proof for a Higgs resonance. These distributions could originate from a spin-2 resonance with an adequate formfactor as well. An analogous formfactor study has been performed previously concerning anomalous Higgs couplings [35]. From now on, the formfactor parameters are set to  $\Lambda_{ff} = 400$  GeV,  $n_{ff} = 3$  throughout this subsection.

On the left hand side of Fig. 7, the impact of the NLO corrections on the transverse momentum of the hardest jet is illustrated. In order to compare the shape, LO distributions are normalized to the LO cross section and NLO distributions to the NLO cross section. The NLO corrections tend to shift the distributions to smaller values of  $p_T$ , since a fraction of the total transverse momentum is carried by the additional gluon in the real emission contribution. This feature is analogous to the SM case [16, 22] and independent of the spin of the resonance. For the spin-0 and spin-2 case, this is depicted in Fig. 7,

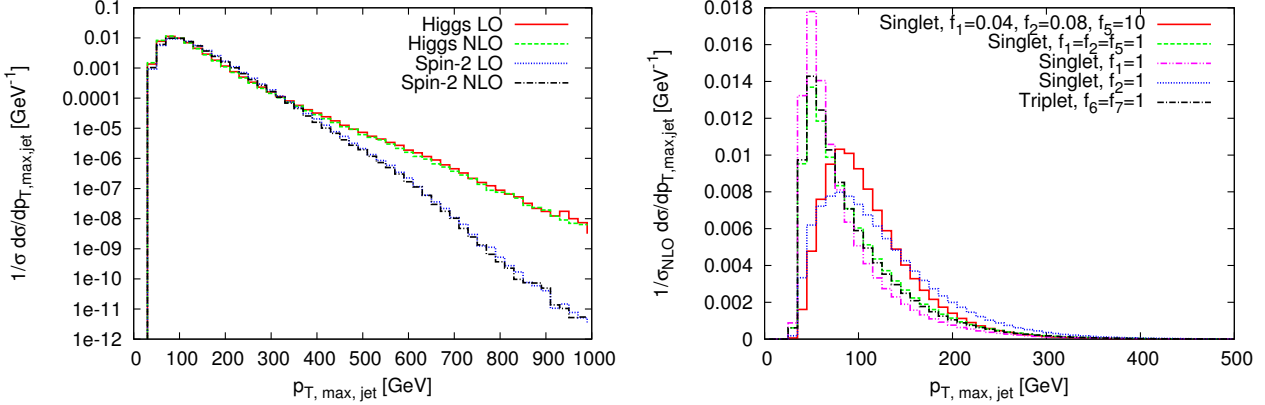


Figure 7: Normalized  $p_T$  distribution of the tagging jet with the largest transverse momentum. Left hand side: Higgs and spin-2 resonance (with  $f_1 = 0.04, f_2 = 0.08, f_5 = 10, f_{i \neq 1,2,5} = 0$ ) at LO and NLO QCD accuracy. Right hand side: Spin-2 singlet and triplet resonance with different coupling parameters at NLO QCD accuracy.

while an analogous plot for spin-1 can be found in Ref. [12]. Due to our scale choice, the impact of the NLO corrections is small, as it is for the integrated cross section as well (see Table 1). While the  $K$ -factor in the high  $p_T$  region ( $400 \text{ GeV} < p_{T, \text{max, jet}} < 900 \text{ GeV}$ ) is around 0.9 for the spin-2 case with  $\mu_F = \mu_R = Q$ , it would be around 0.6 if we had chosen  $\mu_F = \mu_R = m_W$  instead, mainly because of a higher prediction for the LO cross section.

The  $p_T$  distributions of a spin-2 resonance depend slightly on the coupling parameters, which is exemplified on the right hand side of Fig. 7 for the transverse momentum of the hardest jet. This can be understood from the Feynman rules (Eq. 2.8): For  $f_1 = 1, f_{i \neq 1} = 0$ , spin-2 resonances are mainly produced by initial photons, which leads to an enhancement of the low  $p_T$  region, while for the cases  $f_2 = 1, f_{i \neq 2} = 0$  and  $f_1 = 0.04, f_2 = 0.08, f_5 = 10$ , initial  $W$  and  $Z$  bosons dominate. It can also be seen that the  $p_T$  distributions of the spin-2 triplet resonance can be adjusted to those of the Higgs with appropriate formfactor settings.

#### 4.1.2 Angular distributions

In this section, various angular distributions are compared for a Higgs and a spin-2 resonance and for different spin-2 couplings. Furthermore, the impact of the NLO QCD corrections is illustrated. If not indicated otherwise, distributions are presented at NLO QCD accuracy. Note that all the figures include a normalization factor  $1/\sigma_{\text{NLO}}$ .

First, we analyze the azimuthal angle difference between the two tagging jets. This observable has the capability to distinguish between different structures of  $HVV$  couplings [9, 35]. Fig. 8 depicts the respective distribution for a SM Higgs and a spin-2 singlet resonance at LO and NLO QCD accuracy. In both cases, the characteristic shape of the distribution is not modified by the NLO corrections, the curves are just slightly shifted according to the overall  $K$ -factor (see Table 1).

Different spin-2 couplings lead to a slightly different  $\Delta\Phi_{jj}$  distribution of a spin-2 singlet resonance (left hand side of Fig. 9), yet its characteristic shape is nearly indepen-

dent of these parameters. As shown on the right hand side of Fig. 9, the  $\Delta\Phi_{jj}$  distribution of the spin-2 triplet case resembles the singlet case with coupling parameters  $f_1 = 2, f_2 = f_5 = 1, f_{i \neq 1,2,5} = 0$ . Different settings of the triplet couplings hardly influence the distribution, since the contribution of  $f_6$  is negligible. In fact, this is the case for all angular distributions considered. All in all, the  $\Delta\Phi_{jj}$  distribution shows a fundamental difference between a Higgs and a spin-2 resonance, which is nearly independent of the spin-2 coupling parameters. Therefore, it provides an important tool to distinguish between the two resonances.

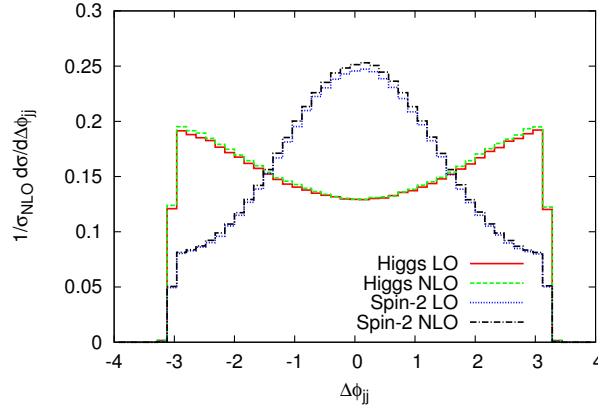


Figure 8: Azimuthal angle difference between the two tagging jets for a Higgs and for a spin-2 resonance with couplings  $f_1 = 0.04, f_2 = 0.08, f_5 = 10, f_{i \neq 1,2,5} = 0$ , both at LO and NLO QCD accuracy.

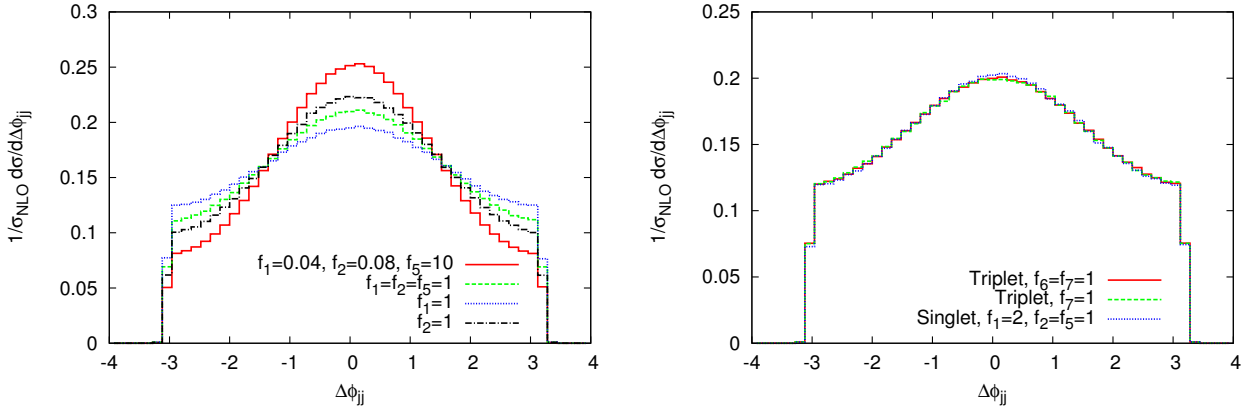


Figure 9: Azimuthal angle difference between the two tagging jets for a spin-2 resonance with different coupling parameters at NLO QCD accuracy. Left hand side: spin-2 singlet, right hand side: spin-2 singlet and triplet.

Another interesting variable is  $\Theta$ , the angle between the momentum of an initial electroweak boson and an outgoing photon in the rest frame of the resonance. Since the dependence of the matrix element on  $\Theta$  is described by the Wigner  $d$ -functions  $d_{m,m'}^j(\Theta)$ ,

even for off-shell incoming vector bosons [36], the  $\cos \Theta$  distribution should be an indicator of the spin of the resonance. The momenta of the initial electroweak bosons are reconstructed from those of the final-state photons and jets. In particular, the jets are assigned to the initial quarks according to their rapidities, assuming that mainly forward scattering takes place. Similar to  $\Delta\Phi_{jj}$ , the  $\cos \Theta$  distribution features a difference between a Higgs and a spin-2 resonance (Fig. 10), which is rather independent of the spin-2 couplings (Fig. 11). Therefore, it is another appropriate distribution for a distinction between the two cases of resonances. The NLO corrections again only shift the distributions slightly, without modifying their characteristic shapes, which is illustrated in Fig. 10.

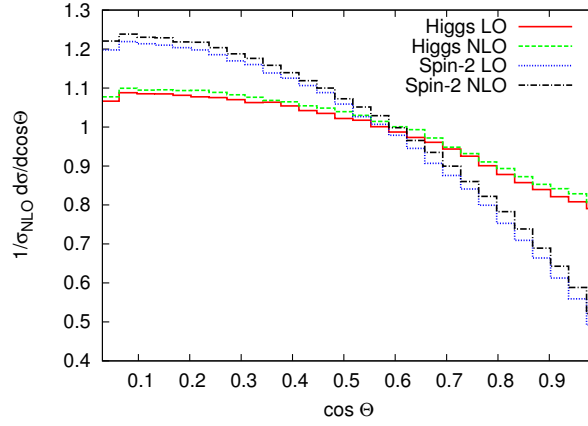


Figure 10: Normalized  $\cos \Theta$  distribution for a Higgs and for a spin-2 resonance with couplings  $f_1 = 0.04, f_2 = 0.08, f_5 = 10, f_{i \neq 1,2,5} = 0$ , both at LO and NLO QCD accuracy.  $\Theta$  is the angle between the reconstructed momentum of an initial electroweak boson and an outgoing photon in the rest frame of the resonance.

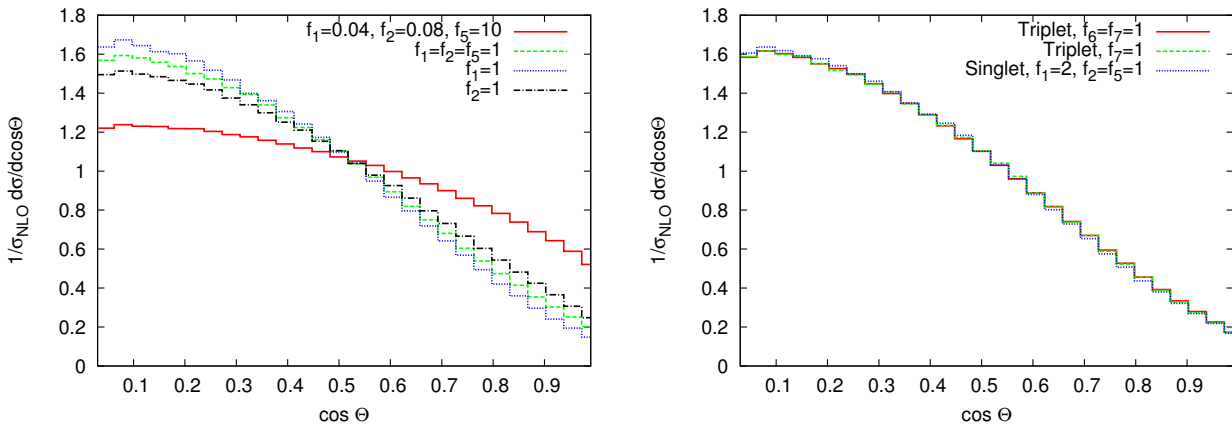


Figure 11: Normalized  $\cos \Theta$  distribution for a spin-2 resonance with different coupling parameters at NLO QCD accuracy. Left hand side: spin-2 singlet, right hand side: spin-2 singlet and triplet.



Analogous to the  $\cos \Theta$  distribution, we analyzed  $\cos \Theta_{j1,2}$  distributions, where  $\Theta_{j1,2}$  is the angle between a final-state photon and the first or second tagging jet in the rest frame of the resonance. They have characteristics similar to the  $\cos \Theta$  distribution: The distributions of a spin-2 resonance are always significantly more central than those of the Higgs and they depend slightly on the coupling parameters.

In Fig. 12 we present another distribution which can be used for a spin-determination of the resonance: The cosine of the Gottfried-Jackson angle, which is the angle between the momentum of the spin-2 particle or the Higgs in the laboratory frame and a final-state photon in the rest frame of the resonance. It differs significantly between a Higgs and a spin-2 resonance and depends even less on the spin-2 couplings (Fig. 13) than the previous distributions.

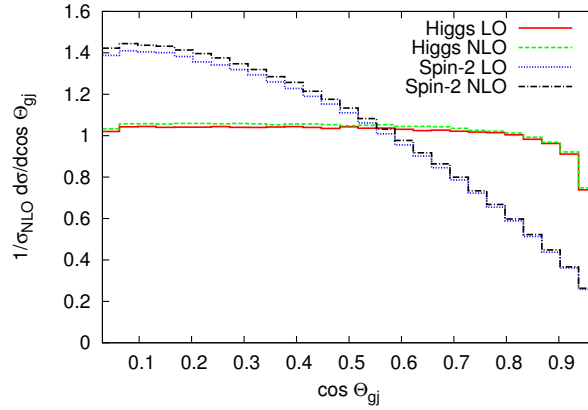


Figure 12: Distribution of the cosine of the Gottfried-Jackson angle for a Higgs and for a spin-2 resonance with couplings  $f_1 = 0.04, f_2 = 0.08, f_5 = 10, f_{i \neq 1,2,5} = 0$ , both at LO and NLO QCD accuracy.

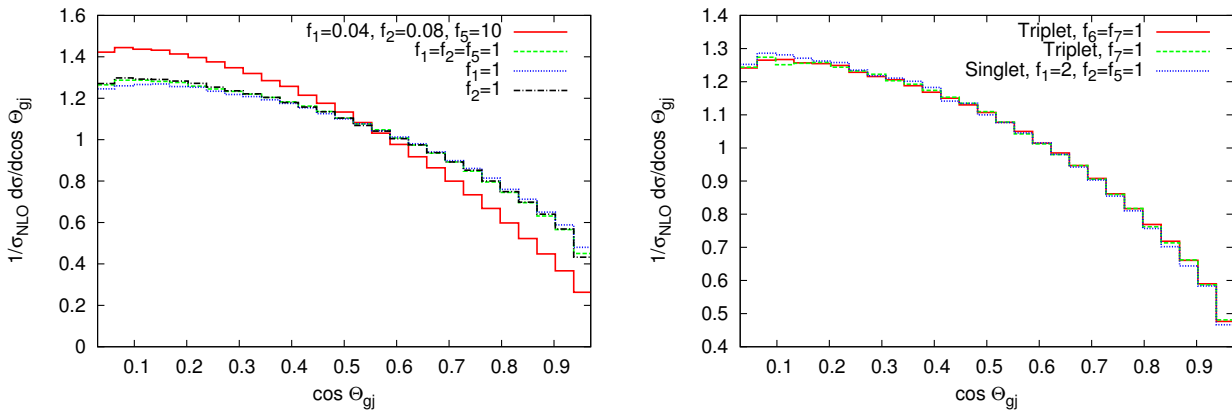


Figure 13: Distribution of the cosine of the Gottfried-Jackson angle for a spin-2 resonance with different coupling parameters at NLO QCD accuracy. Left hand side: spin-2 singlet, right hand side: spin-2 singlet and triplet.

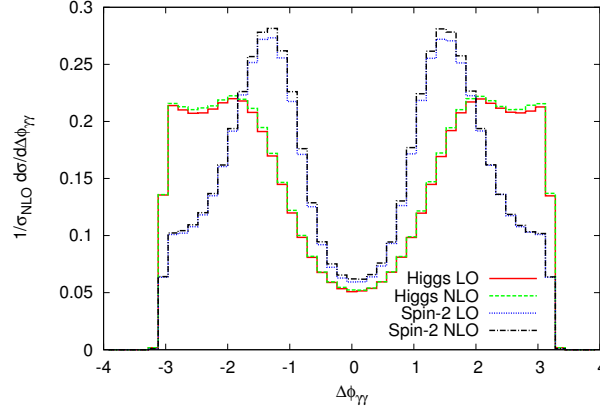


Figure 14: Azimuthal angle difference between the two photons for a Higgs and for a spin-2 resonance with couplings  $f_1 = 0.04, f_2 = 0.08, f_5 = 10, f_{i \neq 1,2,5} = 0$ , both at LO and NLO QCD accuracy.

In contrast to the distributions presented before, the azimuthal angle difference between the two final-state photons differs not only between a Higgs and a spin-2 resonance (Fig. 14), but also between different spin-2 couplings (Fig. 15). Therefore, the  $\Delta\Phi_{\gamma\gamma}$  distribution is not sufficient for a spin-determination of the resonance but, together with other distributions, it can provide useful information about a potential spin-2 resonance and its parameters.

We have also investigated several other distributions, such as the rapidity distributions of the tagging jets, which are typically analyzed for VBF processes, yet none of them revealed any characteristic features for Higgs and spin-2 resonances.

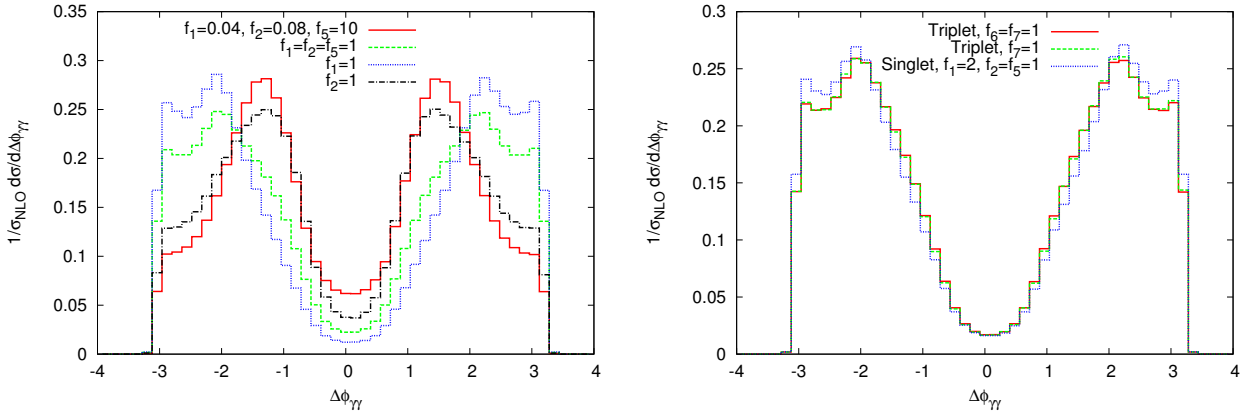


Figure 15: Azimuthal angle difference between the two photons for a spin-2 resonance with different coupling parameters at NLO QCD accuracy. Left hand side: spin-2 singlet, right hand side: spin-2 singlet and triplet.

## 4.2 Heavy Spin-2 resonances in VBF processes with four final-state leptons

In this section, heavy spin-2 resonances in VBF processes with four leptons and two jets in the final state are investigated. Thereby, we consider the different leptonic final states  $e^+ e^- \mu^+ \mu^-$ ,  $e^+ e^- \nu_\mu \bar{\nu}_\mu$ ,  $e^+ \nu_e \mu^- \bar{\nu}_\mu$ ,  $e^+ \nu_e \mu^+ \mu^-$  and  $e^- \bar{\nu}_e \mu^+ \mu^-$ . We mainly focus on  $e^+ e^- \mu^+ \mu^-$ , since a resonance in the invariant-mass spectrum of the leptons can be reconstructed exactly if the final state does not contain a neutrino. We compare the cross sections of the different processes with and without spin-2 resonances, present the characteristic transverse-momentum and angular distributions and study the impact of the NLO QCD corrections on these processes. Furthermore, we investigate how the spin-2 singlet and triplet case, as well as different coupling parameters, can be distinguished from one another.

If not indicated otherwise, we consider a spin-2 singlet resonance with couplings  $f_1 = f_2 = f_5 = 1$ ,  $f_{i \neq 1,2,5} = 0$ ,  $\Lambda = 1.5 \text{ TeV}$  and a mass of 1 TeV. The parameters of the formfactor are  $\Lambda_{ff} = 3 \text{ TeV}$ ,  $n_{ff} = 4$ . For the triplet case, we use the same parameters, apart from the couplings, which are  $f_6 = f_7 = 1$ ,  $f_{i \neq 6,7} = 0$ . Throughout this section, we assume a centre of mass energy of 14 TeV and we set the mass of the Higgs boson to 130 GeV, yet the results do not change for slightly different masses such as 126 GeV. Thus, we are considering models with a heavy spin-2 resonance in addition to a Higgs-like state near 126 GeV.

Final-state leptons	Scenario	LO cross section [fb]	NLO cross section [fb]
$e^+ e^- \mu^+ \mu^-$	SM without spin-2	0.0520	0.0549
	Spin-2 singlet	0.0541	0.0567
	Spin-2 triplet	0.0523	0.0557
$e^+ e^- \nu_\mu \bar{\nu}_\mu$	SM without spin-2	0.203	0.212
	Spin-2 singlet	0.215	0.226
	Spin-2 triplet	0.212	0.224
$e^+ \nu_e \mu^- \bar{\nu}_\mu$	SM without spin-2	2.207	2.278
	Spin-2 singlet	2.249	2.297
	Spin-2 triplet	2.200	2.267
$e^+ \nu_e \mu^+ \mu^-$	SM without spin-2	0.1726	0.1795
	Spin-2 singlet	0.1720	0.1792
	Spin-2 triplet	0.1734	0.1805
$e^- \bar{\nu}_e \mu^+ \mu^-$	SM without spin-2	0.0946	0.1001
	Spin-2 singlet	0.0943	0.1000
	Spin-2 triplet	0.0951	0.1005

Table 2: Integrated cross sections with and without spin-2 resonances for different VBF processes with four final-state leptons at LO and NLO QCD accuracy. The cuts of Section 3.1 are applied. The parameter settings of the spin-2 particles can be found at the beginning of Section 4.2.

Table 2 gives a comparison of the integrated cross sections for the different processes with four leptons and two jets in the final state with and without spin-2 resonances at LO and NLO QCD accuracy. Note that for a given process, these cross sections correspond to a specific leptonic final state. The cross sections for all the possible combinations of lepton generations together can be obtained by multiplying the given cross sections with an appropriate multiplicity factor. For some of the final states, there is some interference between different processes, but this interference is insignificant. One such example is  $e^+ e^- \nu_e \bar{\nu}_e$ , which can be generated both as  $(e^+ e^-)(\nu_e \bar{\nu}_e)$  and as  $(e^+ \nu_e)(e^- \bar{\nu}_e)$ , where the brackets group the fermions into pairs connected by a continuous fermion line. The first case gives rise to events with  $m_{e^+ e^-} \approx m_Z \approx m_{\nu_e \bar{\nu}_e}$ , while the second case has  $m_{e^+ \nu_e} \approx m_W \approx m_{e^- \bar{\nu}_e}$ .

As in the photon pair-production process, the NLO corrections are relatively small, with  $K$ -factors around 1.05. The statistical errors of the total cross sections in Table 2 are at the half percent level. Spin-2 resonances lead to a relative enhancement of the cross section, which is larger for  $pp \rightarrow e^+ e^- \mu^+ \mu^- jj$  and  $pp \rightarrow e^+ e^- \nu_\mu \bar{\nu}_\mu jj$  than for the other processes, i.e. the relative contribution of the continuum  $ZZ$  background is smaller than for the  $WW$  or  $WZ$  cases. For  $pp \rightarrow e^+ \nu_e \mu^+ \mu^- jj$  and  $pp \rightarrow e^- \bar{\nu}_e \mu^+ \mu^- jj$ , there is no singlet resonance, since only the charged resonances of a spin-2 triplet can be produced in these processes. The spin-2 triplet leads to a weaker enhancement than the singlet scenario throughout, corresponding to a narrower resonance, as shown in Table 3. It should be noted, however, that the widths given in this table are fairly arbitrary and merely reflect the parameter choices made above. By increasing the  $f_i$  by a factor of 5 or, equivalently, dropping the scale  $\Lambda$  from 1 TeV to 200 GeV, all partial and total widths and also the spin-2 resonance contributions to the cross sections in Table 2 would increase by a factor of 25, making them much more readily observable. Finally we note that for  $f_1 = f_2$  the decay of the spin-2 resonance to photon pairs is as important as the decay into  $ZZ$ , but the former does not suffer from the small leptonic branching ratios of  $Z$  decay, which is the culprit for the small  $e^+ e^- \mu^+ \mu^-$  rates in Table 2.

#### 4.2.1 The process $pp \rightarrow VV jj \rightarrow e^+ e^- \mu^+ \mu^- jj$

Fig. 16 depicts the invariant-mass distribution of the four final-state leptons for the process  $pp \rightarrow VV jj \rightarrow e^+ e^- \mu^+ \mu^- jj$ , which can be fully reconstructed experimentally since there are no neutrinos in the final state. For the Standard Model, a Higgs resonance at 126 GeV is followed by a continuous distribution which vanishes for high energies. The spin-2 singlet resonance peak is shown for different masses up to 1.5 TeV for the given parameter settings. The triplet case is analogous, except for the height and width of the resonance, which is chosen to have a mass of 1 TeV. The triplet resonance is generated by the neutral spin-2 triplet particle in this process. Due to the formfactor, there are no unphysical high-energy contributions outside the depicted mass range, which otherwise would result from unitarity violation. For a mass of 500 GeV, these contributions are not suppressed completely for  $\Lambda_{ff} = 3$  TeV. For such small masses, a smaller value of  $\Lambda_{ff}$  should be chosen. The total widths of the spin-2 resonances shown in Fig. 16 are given in Table 3.

In Figs. 17 to 20, we present the characteristic transverse-momentum and angular

Resonance	Width [GeV]
Singlet, 500 GeV	0.982
Singlet, 750 GeV	3.238
Singlet, 1000 GeV	7.607
Singlet, 1250 GeV	14.795
Singlet, 1500 GeV	25.505
Triplet, 1000 GeV	1.004

Table 3: Total widths of the spin-2 resonances shown in Fig. 16.

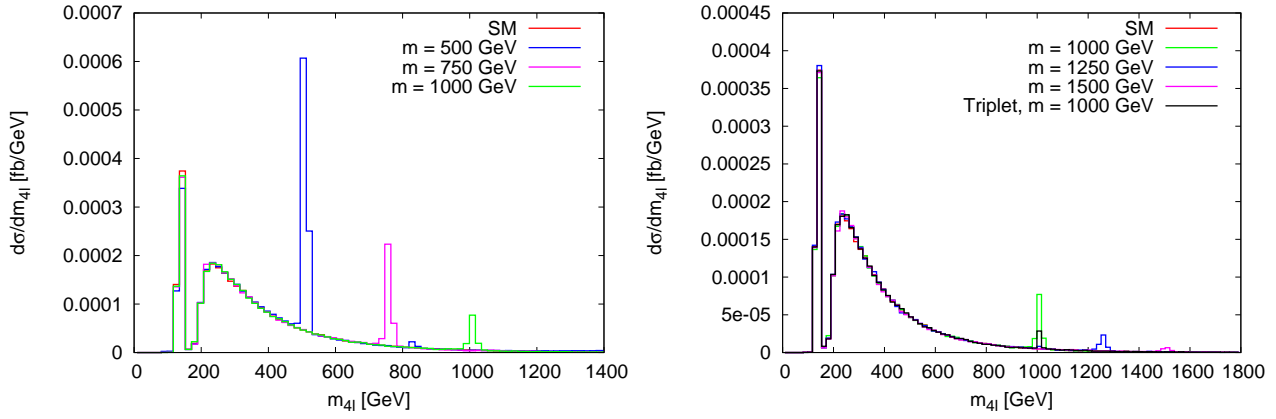


Figure 16: Invariant-mass distribution of the four final-state leptons: Spin-2 singlet and triplet resonances with different masses in the process  $pp \rightarrow VV jj \rightarrow e^+ e^- \mu^+ \mu^- jj$  at NLO QCD accuracy.

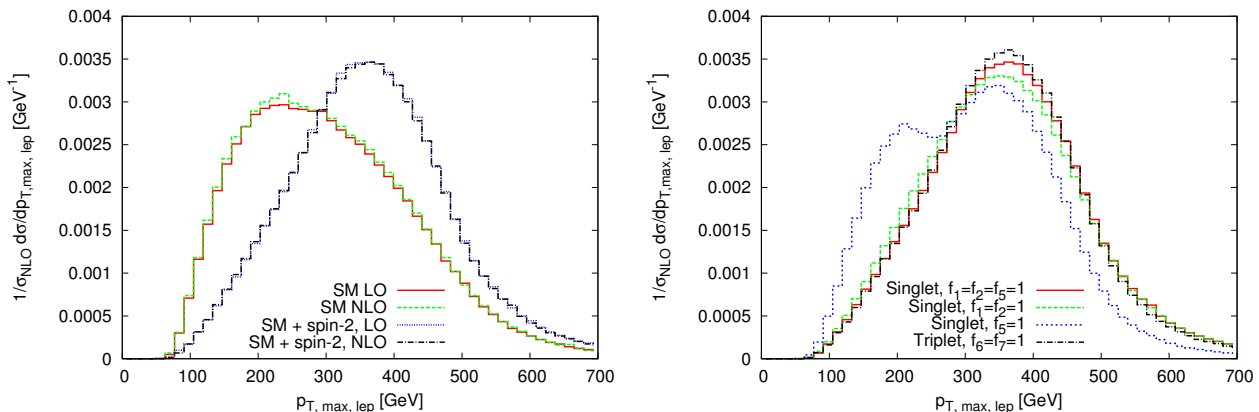


Figure 17: Transverse-momentum distribution of the hardest final-state lepton for events near the spin-2 resonance (see text for details). Left hand side: With and without a spin-2 singlet resonance with couplings  $f_1 = f_2 = f_5 = 1$  at LO and NLO QCD accuracy. Right hand side: Spin-2 singlet and triplet resonance with different coupling parameters at NLO accuracy. The electroweak continuum contributions as mentioned in Section 3 are always included.

distributions of spin-2 singlet and triplet resonances at 1 TeV. We have selected those distributions which show the most prominent differences between the different models. The left hand sides depict the distributions for a spin-2 singlet resonance (including the electroweak continuum in a mass bin around the resonance) and of the SM continuum expectation, without such a resonance, at LO and NLO QCD accuracy, whereas the right hand sides compare the singlet and triplet case and different coupling parameters at NLO QCD accuracy, again including the electroweak continuum in all cases. All the figures are normalized to the NLO cross sections. In order to reveal the features of the spin-2 resonances, additional cuts on the invariant mass of the four leptons are applied. For the parameter settings  $f_1 = f_2 = f_5 = 1$ ,  $f_1 = f_2 = 1$  and for the SM without a spin-2 resonance, they are chosen as  $m_{4l} = 1000 \pm 50$  GeV. For the triplet case, we use  $m_{4l} = 1000 \pm 10$  GeV and for  $f_5 = 1$ , we set  $m_{4l} = 1000 \pm 5$  GeV. The latter cases are only presented for illustration, since the experimental resolution is expected to be worse. However, for larger couplings  $f_i/\Lambda$  and resulting larger production rates of the spin-2 resonances, the characteristic distributions would be visible for wider mass bins. With these additional cuts, we obtain a signal-to-background ratio of approximately one for the case  $f_5 = 1$ , approximately three for  $f_1 = f_2 = 1$  and approximately four in the other cases. Here “background” refers to the expected electroweak continuum contribution from VBF within the SM.

Characteristic differences between a spin-2 resonance and the SM background arise especially in the distribution of the transverse momentum of the hardest final-state lepton (Fig. 17), the azimuthal angle difference between the two tagging jets (Fig. 18), the cosine of the angle between the momenta of an incoming and an outgoing electroweak boson in the rest frame of the spin-2 resonance (or of the four final-state leptons, respectively) (Fig. 19) and the pseudorapidity difference between the two positively charged final-state leptons (Fig. 20). The NLO corrections do not have any significant impact on cross

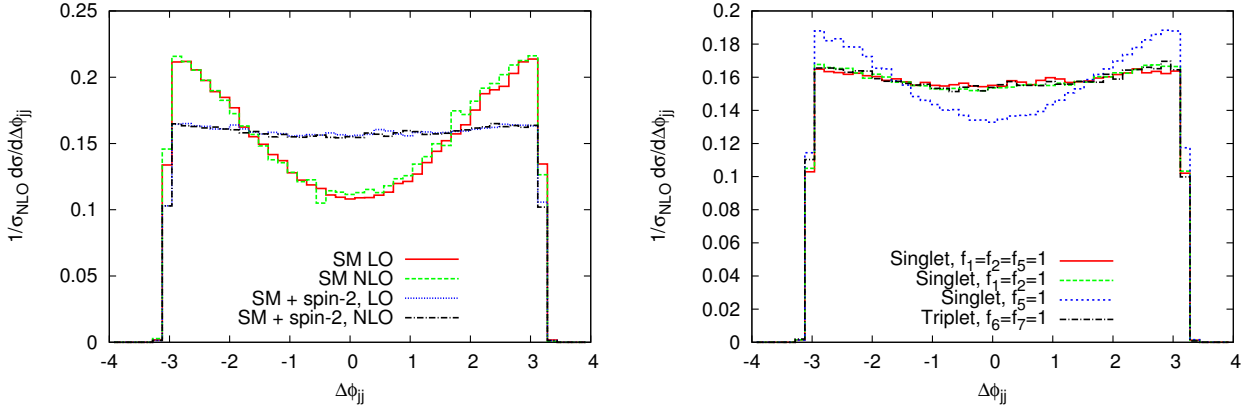


Figure 18: Azimuthal angle difference between the two tagging jets. Parameters for the different cases are as in Fig. 17.

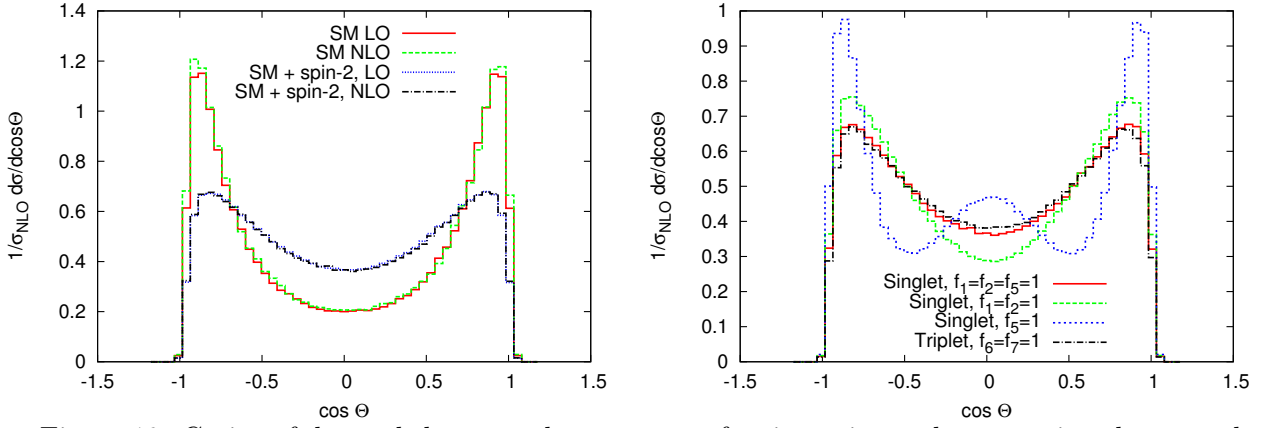


Figure 19: Cosine of the angle between the momenta of an incoming and an outgoing electroweak boson in the rest frame of the spin-2 resonance. Parameters for the different cases are as in Fig. 17.

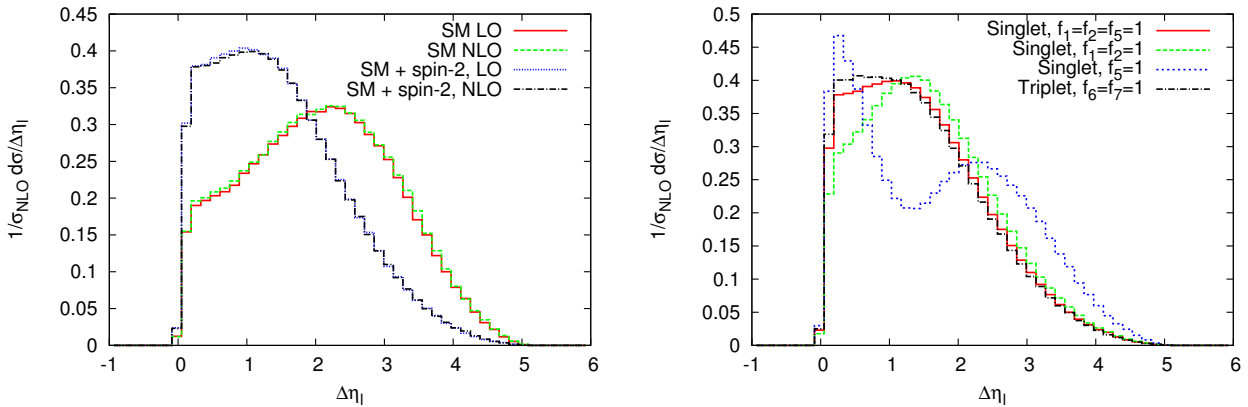


Figure 20: Pseudorapidity difference between the two positively charged final-state leptons. Parameters for the different cases are as in Fig. 17.

sections and distributions in the high invariant-mass region studied here. A spin-2 triplet resonance resembles a singlet resonance with couplings  $f_1 = f_2 = f_5 = 1$ . The cases  $f_1 = f_2 = f_5 = 1$  and  $f_1 = f_2 = 1$  are difficult to distinguish since, numerically, the  $f_5$  contribution is sub-dominant. However, small differences are visible in the  $\cos \Theta$  and  $\Delta\eta_l$  distributions and they do not only stem from contamination of the electroweak continuum. The coupling  $f_5$  alone leads to different distributions throughout. This is not simply an effect of the sizable electroweak continuum background for small  $f_5/\Lambda$ , but reflects the different tensor structure, as we have verified by comparing with the case  $f_5 = 10$ . For  $f_5 = 10$ , the  $\Delta\Phi_{jj}$  distribution approaches those of the other spin-2 cases, while for the  $\cos \Theta$  distribution the peak around  $\cos \Theta = 0$  becomes more prominent.

Note that the  $\cos \Theta$  distribution of Fig. 19 is not accessible experimentally for processes with final-state neutrinos. However, since for this figure the momenta of the electroweak bosons were not reconstructed from final-state momenta, as in Section 4.1, but taken directly from the Monte Carlo information, the results can be directly taken over for final states with neutrinos. Besides  $\cos \Theta$ , we have also studied the  $\cos \Theta_{j1,2}$  distributions, where  $\Theta_{j1,2}$  is the angle between the momenta of an outgoing electroweak boson and the first or second tagging jet in the rest frame of the spin-2 resonance (or of the four final-state leptons, respectively). These distributions show a behaviour similar to  $\cos \Theta$ .

#### 4.2.2 Other processes with four final-state leptons

The VBF process  $pp \rightarrow VV jj \rightarrow e^+ e^- \nu_\mu \bar{\nu}_\mu jj$  is very similar to  $pp \rightarrow VV jj \rightarrow e^+ e^- \mu^+ \mu^- jj$ , which was analyzed in the previous section. Theoretically, a spin-2 resonance in the invariant four-lepton mass spectrum as well as the transverse-momentum and angular distributions with a cut on the invariant four-lepton mass look the same, despite the fact that there is no use in investigating the angular distributions of the two charged leptons, since they emerge from the same vector boson in this case. However, since the invariant four-lepton mass cannot be reconstructed experimentally, the transverse mass of the lepton system  $e^+ e^- \nu_\mu \bar{\nu}_\mu$  has to be considered instead, which is defined as [37]:

$$m_T = \sqrt{(E_{T,l} + E_{T,\text{miss}})^2 - (\mathbf{p}_{T,l} + \mathbf{p}_{T,\text{miss}})^2}, \quad (4.1)$$

with

$$E_{T,l} = \sqrt{\mathbf{p}_{T,l}^2 + m_Z^2}, \quad E_{T,\text{miss}} = \sqrt{\mathbf{p}_{T,\text{miss}}^2 + m_Z^2}, \quad (4.2)$$

where  $E_{T,l}, \mathbf{p}_{T,l}$  denote the transverse energy and momentum of the two charged leptons and  $E_{T,\text{miss}}, \mathbf{p}_{T,\text{miss}}$  those of the neutrino system.

Although an excess from the spin-2 resonance is hardly visible in the transverse-mass spectrum for our choice of parameters, some of the characteristics of the differential distributions remain accessible if a transverse-mass cut, e.g.  $m_T = 1000 \pm 100$  GeV, is applied instead of the cut on the invariant four-lepton mass. Whereas the difference in the transverse momentum of the hardest lepton (left hand side of Fig. 17) disappears, the azimuthal angle difference of the two tagging jets (Fig. 18) remains the same.

In the process  $pp \rightarrow W^+ W^- jj \rightarrow e^+ \nu_e \mu^- \bar{\nu}_\mu jj$ , it is even harder to access the characteristics of spin-2 resonances, since  $t\bar{t}$  + jets constitute a large background to this



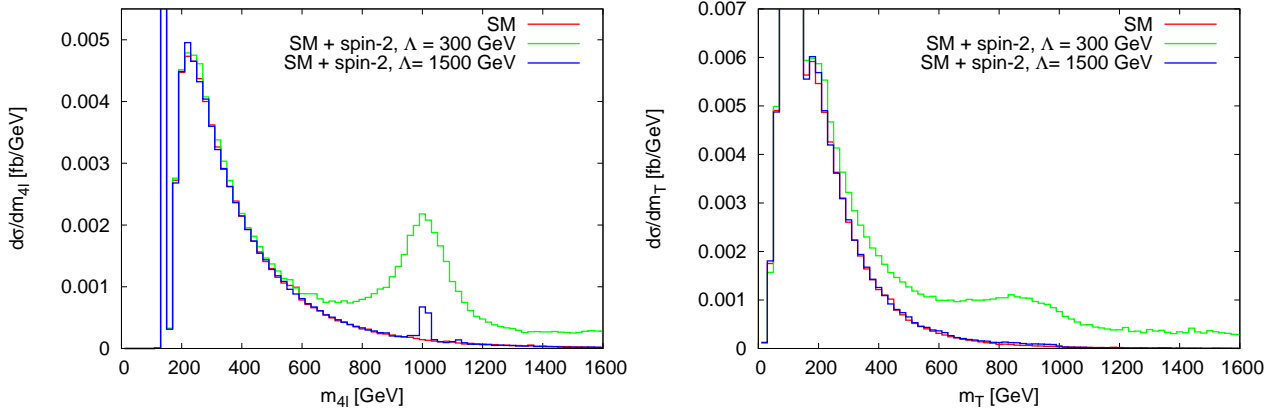


Figure 21: Process  $pp \rightarrow W^+W^- jj \rightarrow e^+ \nu_e \mu^- \bar{\nu}_\mu jj$  with and without a spin-2 singlet resonance for different values of  $\Lambda$ . Left hand side: Invariant mass of the four final-state leptons, right hand side: Transverse mass, at NLO QCD accuracy.

process at the LHC. Furthermore, the spin-2 singlet resonance is smaller than in the processes analyzed before (see Fig. 21) and the triplet resonance is even smaller, since the uncharged triplet particle couples to two  $W$  bosons only via the  $f_6$  term, whereas the Feynman rules for vertices involving photons and  $Z$  bosons contain the coupling  $f_7$  (see Eq. 2.10). Again, the invariant four-lepton mass is not accessible experimentally and the transverse mass of the system  $e^+ \nu_e \mu^- \bar{\nu}_\mu$  has to be considered instead. For this process, it is defined as in Eq. 4.1, but with [16]

$$E_{T,l} = \sqrt{\mathbf{p}_{T,l}^2 + m_l^2}, \quad E_{T,\text{miss}} = \sqrt{\mathbf{p}_{T,\text{miss}}^2 + m_{\nu\nu}^2} \rightarrow |\mathbf{p}_{T,\text{miss}}|, \quad (4.3)$$

where  $m_l$  is the invariant mass of the charged-lepton system.

Fig. 21 compares spin-2 singlet resonances for different values of  $\Lambda$  in the (only theoretically accessible) four-lepton invariant mass and the transverse-mass distribution. Here, the high Higgs resonance peak is cut off in order to concentrate on the spin-2 resonance region. For the usual parameter settings, with  $\Lambda = 1.5$  TeV, the transverse-mass spectrum is roughly the same for the SM with and without a spin-2 resonance. Even for  $\Lambda$  as small as 300 GeV (or large couplings  $f_i$ , respectively), the resonance is very smeared out. The characteristics of the transverse-momentum and angular distributions, which are theoretically similar to those of the process  $pp \rightarrow VV jj \rightarrow e^+ e^- \mu^+ \mu^- jj$ , remain accessible with a transverse-mass cut if the couplings are not too small. For the usual settings, with  $\Lambda = 1.5$  TeV, the differences between the SM and a model with a spin-2 singlet resonance are small and very difficult to observe in the  $W^+W^-$  mode at the LHC.

In the processes  $pp \rightarrow VV jj \rightarrow e^+ \nu_e \mu^+ \mu^- jj$  and  $pp \rightarrow VV jj \rightarrow e^- \bar{\nu}_e \mu^+ \mu^- jj$ , only charged resonances are possible. Therefore, there can be a spin-2 triplet resonance generated by the charged triplet particle, but no singlet resonance. Again, this resonance can only be reconstructed in Monte Carlo in the invariant four-lepton mass spectrum and the features of the distributions with a cut on the invariant four-lepton mass are as usual. The corresponding transverse mass in this case reads [37]:

$$m_T = \sqrt{(E_{T,l} + E_{T,\text{miss}})^2 - (\mathbf{p}_{T,l} + \mathbf{p}_{T,\text{miss}})^2}, \quad (4.4)$$

with

$$E_{T,\ell\ell} = \sqrt{\mathbf{p}_{T,\ell\ell}^2 + m_{\ell\ell}^2}, \quad E_{T,\text{miss}} = |\mathbf{p}_{T,\text{miss}}|, \quad (4.5)$$

where  $m_{\ell\ell}$  denotes the invariant mass of the charged-lepton system,  $E_{T,\ell\ell}, \mathbf{p}_{T,\ell\ell}$  its transverse energy and momentum and  $E_{T,\text{miss}}, \mathbf{p}_{T,\text{miss}}$  those of the neutrino.

The spin-2 triplet resonance peak can be observed in the transverse-mass spectrum if the couplings are not too small. However, we find that the parameters chosen above yield a marginal signal only. With a transverse-mass cut of  $m_T = 1000 \pm 100$  GeV, the characteristics of distributions, such as the pseudorapidity difference between two final-state leptons of the same charge, can be studied and yield results similar to those found for final states with four charged leptons.

## 5 Conclusions

We have studied spin-2 resonances in vector-boson-fusion processes at the LHC within the framework of an effective model describing the interaction of spin-2 particles with electroweak gauge bosons for a spin-2 singlet and a spin-2 triplet scenario. Unitarity of the underlying vector boson scattering in such models requires the introduction of formfactors which decrease the contribution of spin-2 particle exchange at high energies and which parametrize high-energy contributions beyond this effective model. The calculation was performed within the Monte Carlo program VBFNLO at NLO QCD accuracy. We have analyzed two different kinds of processes: light, Higgs-like spin-2 resonances producing two photons and heavy spin-2 resonances in different four-lepton final states.

For the first process, by using formfactors and adjusting the couplings it is possible to tune the cross section and the transverse-momentum distributions of photons and jets to roughly agree with expectations for the SM Higgs boson of the same mass. Even then, the azimuthal-angle difference between the two tagging jets, as well as the Gottfried-Jackson angle and the angle between an intermediate vector boson and a final-state photon, clearly distinguish between spin-0 and spin-2 resonances. This allows one to separate the two cases and establish the correct spin nature of the observed resonance. Furthermore, the azimuthal-angle difference between the two photons differs if the structure of the contributing operators is changed. This can provide a handle on how a possible spin-2 state is coupled to the gauge bosons.

Among the processes with four leptons and two jets in the final state, namely  $e^+ e^- \mu^+ \mu^- jj$ ,  $e^+ e^- \nu_\mu \bar{\nu}_\mu jj$ ,  $e^+ \nu_e \mu^- \bar{\nu}_\mu jj$ ,  $e^+ \nu_e \mu^+ \mu^- jj$  and  $e^- \bar{\nu}_e \mu^+ \mu^- jj$  production, spin-2 resonances can be observed most cleanly in the first of them, albeit at a very low rate, since the resonance can be reconstructed in the invariant-mass distribution of the four final-state charged leptons. Heavy spin-2 resonances feature characteristic differential distributions, which are observable if the couplings are not too small and a proper cut on the invariant four-lepton mass is applied. The distribution of the transverse momentum of the hardest final-state lepton, the azimuthal angle difference between the two tagging jets, the cosine of the angle between the momenta of an incoming and an outgoing electroweak boson in the rest frame of the spin-2 resonance and the pseudorapidity difference between two final-state leptons are especially useful to identify a spin-2 resonance above the SM

background. In the other processes with four leptons and two jets in the final state, heavy spin-2 resonances are only visible in the transverse-mass spectrum for relatively large spin-2 couplings. However, some characteristics of the differential distributions also remain accessible in the case of smaller couplings if appropriate transverse-mass cuts are applied. In the processes  $pp \rightarrow VV jj \rightarrow e^+ \nu_e \mu^+ \mu^- jj$  and  $pp \rightarrow VV jj \rightarrow e^- \bar{\nu}_e \mu^+ \mu^- jj$ , only charged resonances are possible. Thus, they can be useful to distinguish between the spin-2 singlet and triplet scenarios.

Similar to the SM case, the NLO QCD corrections are small, leading to slightly enhanced cross sections with  $K$ -factors of approximately 1.05 and have no impact on the characteristics of the differential distributions.

## Acknowledgments

This research was supported in part by the Deutsche Forschungsgemeinschaft via the Sonderforschungsbereich/Transregio SFB/TR-9 “Computational Particle Physics” and the Initiative and Networking Fund of the Helmholtz Association, contract HA-101 (“Physics at the Terascale”). J.F. acknowledges support by the “Landesgraduiertenförderung” of the State of Baden-Württemberg.

## A Decay widths of the Spin-2 singlet and triplet particles

### A.1 Singlet

We define the total decay width of the spin-2 singlet particle  $T$  as

$$\Gamma_{\text{total}} = \sum_j \Gamma_j \cdot \frac{1}{b}, \quad (\text{A.1})$$

where the sum runs over the decay channels resulting from the relevant vertices of Sec. 2. The free parameter  $b$ , which is set to 1 in the present analysis, is the fraction of these decays over all possible decays.

The explicit results for the partial decay widths,  $\Gamma_j$ , are:

$$\begin{aligned} \Gamma_{W+W-} = & \left( \frac{24f_2^2(m_T^4 - 3m_T^2m_W^2 + 6m_W^4) + 40f_2f_5g^2v^2(m_T^2 - m_W^2)}{12\Lambda^2} \right. \\ & \left. + \frac{f_5^2g^4v^4(m_T^4 + 12m_T^2m_W^2 + 56m_W^4)}{96\Lambda^2m_W^4} \right) \cdot \frac{\sqrt{(m_T^2/4 - m_W^2)}}{(40\pi m_T^2)} \end{aligned} \quad (\text{A.2})$$

$$\begin{aligned} \Gamma_{ZZ} = & ([24f_2^2c_w^4(m_T^4 - 3m_T^2m_Z^2 + 6m_Z^4) + 8c_w^2f_2(6f_1s_w^2(m_T^4 - 3m_T^2m_Z^2 + 6m_Z^4) \\ & + 5f_5v^2(g^2 + g'^2)(m_T^2 - m_Z^2)) + 24f_1^2s_w^4(m_T^4 - 3m_T^2m_Z^2 + 6m_Z^4)] \end{aligned}$$

$$+ 40f_1f_5s_w^2v^2(g^2 + g'^2)(m_T^2 - m_Z^2)]/(12\Lambda^2) \\ + \frac{f_5^2v^4(g^2 + g'^2)^2(m_T^4 + 12m_T^2m_Z^2 + 56m_Z^4)}{96\Lambda^2m_Z^4} \Big) \cdot \frac{\sqrt{m_T^2/4 - m_Z^2}}{80\pi m_T^2} \quad (\text{A.3})$$

$$\Gamma_{\gamma\gamma} = \frac{(f_1c_w^2 + f_2s_w^2)^2m_T^3}{80\pi\Lambda^2} \quad (\text{A.4})$$

$$\Gamma_{\gamma Z} = \frac{c_w^2s_w^2(f_1 - f_2)^2(m_T^2 - m_Z^2)^3(6m_T^4 + 3m_T^2m_Z^2 + m_Z^4)}{240\pi\Lambda^2m_T^7}, \quad (\text{A.5})$$

where  $m_T$  denotes the mass of the spin-2 singlet particle.

## A.2 Triplet

For the decay width of the neutral and the charged spin-2 triplet particles, the same definition (Eq. (A.1)) is applied. The parameter  $b$  can differ from the singlet case and can be different for the neutral and the charged particles, yet it is set to 1 in the present analysis for all cases.

The following equations present the results for  $\Gamma_j$  for the neutral spin-2 triplet particle:

$$\Gamma_{W^+W^-} = \frac{f_6^2g^4v^4(m_T^4 + 12m_T^2m_W^2 + 56m_W^4)}{384\Lambda^2m_W^4} \cdot \frac{\sqrt{m_T^2/4 - m_W^2}}{40\pi m_T^2} \quad (\text{A.6})$$

$$\Gamma_{ZZ} = \left( (768f_7^2c_w^2s_w^2m_Z^4(m_T^4 - 3m_T^2m_Z^2 + 6m_Z^4) + 640c_wf_6f_7m_Z^4s_wv^2 \right. \\ \left. (g^2 + g'^2)(m_T^2 - m_Z^2) + f_6^2v^4(g^2 + g'^2)^2(m_T^4 + 12m_T^2m_Z^2 + 56m_Z^4) \right) \\ / (384\Lambda^2m_Z^4) \cdot \frac{\sqrt{m_T^2/4 - m_Z^2}}{80\pi m_T^2} \quad (\text{A.7})$$

$$\Gamma_{\gamma\gamma} = \frac{f_7^2c_w^2s_w^2m_T^3}{80\pi\Lambda^2} \quad (\text{A.8})$$

$$\Gamma_{\gamma Z} = \frac{f_7^2(c_w^2 - s_w^2)^2(m_T^2 - m_Z^2)^3(6m_T^4 + 3m_T^2m_Z^2 + m_Z^4)}{960\pi\Lambda^2m_T^7}. \quad (\text{A.9})$$

Here,  $m_T$  denotes the mass of the neutral spin-2 triplet particle.

The partial decay widths of the charged spin-2 particles are:

$$\Gamma_{W\gamma} = \frac{f_7^2c_w^2(m_T^2 - m_W^2)^3(6m_T^4 + 3m_T^2m_W^2 + m_W^4)}{960\pi\Lambda^2m_T^7} \quad (\text{A.10})$$

$$\begin{aligned}
\Gamma_{WZ} = & ((m_T^2 m_W^2 (m_T^2 m_Z^2 (13 f_6^2 g^2 v^4 (g^2 + g'^2) + 256 f_7^2 m_W^2 m_Z^2 s_w^2) \\
& + 1/4 (m_T^2 - m_W^2 + m_Z^2)^2 (7 f_6^2 g^2 v^4 (g^2 + g'^2) - 96 f_7^2 m_W^2 m_Z^2 s_w^2)) \\
& + 1/4 (m_T^2 + m_W^2 - m_Z^2)^2 (m_T^2 m_Z^2 (7 f_6^2 g^2 v^4 (g^2 + g'^2) - 96 f_7^2 m_W^2 m_Z^2 s_w^2) \\
& + (m_T^2 - m_W^2 + m_Z^2)^2 (f_6^2 g^2 v^4 (g^2 + g'^2) + 32 f_7^2 m_W^2 m_Z^2 s_w^2)) \\
& + m_T^2 (m_T^2 - m_W^2 - m_Z^2) (1/4 (m_T^2 + m_W^2 - m_Z^2) (m_T^2 - m_W^2 + m_Z^2) \\
& (128 f_7^2 m_W^2 m_Z^2 s_w^2 - f_6^2 g^2 v^4 (g^2 + g'^2)) + 40 f_6 f_7 g m_T^2 m_W^2 m_Z^2 s_w v^2 \sqrt{g^2 + g'^2}) \\
& + 1/4 m_T^4 (-m_T^2 + m_W^2 + m_Z^2)^2 (f_6^2 g^2 v^4 (g^2 + g'^2) + 32 f_7^2 m_W^2 m_Z^2 s_w^2) \\
& + 40 f_6 f_7 g m_T^2 m_W^2 m_Z^2 s_w v^2 \sqrt{g^2 + g'^2} (m_T^2 + m_W^2 - m_Z^2) \\
& (m_T^2 - m_W^2 + m_Z^2)) / (96 \Lambda^2 m_T^4 m_W^2 m_Z^2)) \\
& \cdot \frac{\sqrt{(m_T^2 - m_W^2 - m_Z^2)^2 - 4 m_W^2 m_Z^2}}{80 \pi m_T^3}, \tag{A.11}
\end{aligned}$$

with  $m_T$  now being the mass of the charged spin-2 triplet particles.

## References

- [1] G. Aad *et al.* [ATLAS Collaboration], Phys. Lett. B **716** (2012) 1.
- [2] S. Chatrchyan *et al.* [CMS Collaboration], Phys. Lett. B **716** (2012) 30.
- [3] P. W. Higgs, Phys. Lett. **12**, 132 (1964), Phys. Rev. Lett. **13**, 508 (1964), Phys. Rev. **145**, 1156 (1966); F. Englert and R. Brout, Phys. Rev. Lett. **13**, 321 (1964); G. S. Guralnik, C. R. Hagen and T. W. B. Kibble, Phys. Rev. Lett. **13**, 585 (1964).
- [4] T. Han, G. Valencia and S. Willenbrock, Phys. Rev. Lett. **69**, 3274 (1992); T. Figy, C. Oleari and D. Zeppenfeld, Phys. Rev. D **68**, 073005 (2003); M. Ciccolini, A. Denner and S. Dittmaier, Phys. Rev. Lett. **99**, 161803 (2007). and Phys. Rev. D **77**, 013002 (2008); P. Bolzoni, F. Maltoni, S. -O. Moch and M. Zaro, Phys. Rev. Lett. **105**, 011801 (2010) and Phys. Rev. D **85**, 035002 (2012).
- [5] S. Chatrchyan *et al.* [CMS Collaboration], Phys. Lett. B **710**, 403 (2012) and HIG-12-015.
- [6] C. P. Burgess, J. Matias and M. Pospelov, Int. J. Mod. Phys. A **17**, 1841 (2002); for discussions on Higgs imposters see W. D. Goldberger, B. Grinstein and W. Skiba, Phys. Rev. Lett. **100**, 111802 (2008) [arXiv:0708.1463 [hep-ph]]; J. Fan, W. D. Goldberger, A. Ross and W. Skiba, Phys. Rev. D **79** (2009) 035017 [arXiv:0803.2040 [hep-ph]]; A. De Rujula, J. Lykken, M. Pierini, C. Rogan and M. Spiropulu, Phys. Rev. D **82**, 013003 (2010); J. Chang, K. Cheung, P. -Y. Tseng and T. -C. Yuan, arXiv:1206.5853 [hep-ph]; I. Low, J. Lykken and G. Shaughnessy, arXiv:1207.1093 [hep-ph]; B. Coleppa, K. Kumar and H. E. Logan, arXiv:1208.2692 [hep-ph]; Z. Chacko, R. Franceschini and R. K. Mishra, arXiv:1209.3259 [hep-ph].

- [7] D. Zeppenfeld, R. Kinnunen, A. Nikitenko and E. Richter-Was, Phys. Rev. D **62**, 013009 (2000); M. Dührssen, S. Heinemeyer, H. Logan, D. Rainwater, G. Weiglein and D. Zeppenfeld, Phys. Rev. D **70**, 113009 (2004); R. Lafaye, T. Plehn, M. Rauch, D. Zerwas and M. Duhrssen, JHEP **0908**, 009 (2009); M. Rauch, arXiv:1110.1196 [hep-ph]; F. Bonnet, M. B. Gavela, T. Ota and W. Winter, Phys. Rev. D **85**, 035016 (2012); D. Carmi, A. Falkowski, E. Kuflik and T. Volansky, JHEP **1207**, 136 (2012) and arXiv:1206.4201; D. Carmi, A. Falkowski, E. Kuflik, T. Volansky and J. Zupan, arXiv:1207.1718; P. P. Giardino, K. Kannike, M. Raidal and A. Strumia, JHEP **1206**, 117 (2012) and arXiv:1207.1347; J. Ellis and T. You, JHEP **1206**, 140 (2012) and JHEP **1209**, 123 (2012); J. R. Espinosa, C. Grojean, M. Mühlleitner and M. Trott, JHEP **1205**, 097 (2012) and JHEP **1209**, 126 (2012) and arXiv:1207.1717; A. Azatov, R. Contino and J. Galloway, JHEP **1204**, 127 (2012); A. Azatov, R. Contino, D. Del Re, J. Galloway, M. Grassi and S. Rahatlou, JHEP **1206**, 134 (2012); M. Klute, R. Lafaye, T. Plehn, M. Rauch and D. Zerwas, Phys. Rev. Lett. **109**, 101801 (2012); T. Corbett, O. J. P. Eboli, J. Gonzalez-Fraile and M. C. Gonzalez-Garcia, arXiv:1207.1344 [hep-ph]; R. S. Gupta, H. Rzehak and J. D. Wells, Phys. Rev. D **86**, 095001 (2012); S. Banerjee, S. Mukhopadhyay and B. Mukhopadhyaya, arXiv:1207.3588 [hep-ph]; F. Bonnet, T. Ota, M. Rauch and W. Winter, arXiv:1207.4599 [hep-ph]; T. Plehn and M. Rauch, arXiv:1207.6108 [hep-ph]; ATLAS Collaboration, ATLAS-CONF-2012-127; A. Djouadi, arXiv:1208.3436 [hep-ph]; B. A. Dobrescu and J. D. Lykken, arXiv:1210.3342 [hep-ph]; G. Moreau, arXiv:1210.3977 [hep-ph]; E. Masso and V. Sanz, arXiv:1211.1320 [hep-ph].
- [8] A. Djouadi, W. Kilian, M. Muhlleitner and P. M. Zerwas, Eur. Phys. J. C **10**, 45 (1999); U. Baur, T. Plehn and D. L. Rainwater, Phys. Rev. Lett. **89**, 151801 (2002); U. Baur, T. Plehn and D. L. Rainwater, Phys. Rev. D **67**, 033003 (2003); A. Dahlhoff, arXiv:hep-ex/0505022; U. Baur, T. Plehn and D. L. Rainwater, Phys. Rev. D **69**, 053004 (2004); T. Plehn and M. Rauch, Phys. Rev. D **72**, 053008 (2005); T. Binoth, S. Karg, N. Kauer and R. Rückl, Phys. Rev. D **74**, 113008 (2006); M. J. Dolan, C. Englert and M. Spannowsky, arXiv:1206.5001 [hep-ph].
- [9] T. Plehn, D. L. Rainwater and D. Zeppenfeld, Phys. Rev. Lett. **88**, 051801 (2002); S. Y. Choi, D. J. Miller, 2, M. M. Muhlleitner and P. M. Zerwas, Phys. Lett. B **553**, 61 (2003); C. P. Buszello, I. Fleck, P. Marquard and J. J. van der Bij, Eur. Phys. J. C **32**, 209 (2004); V. Hankele, G. Klämke and D. Zeppenfeld, arXiv:hep-ph/0605117; G. Klämke and D. Zeppenfeld, JHEP **0704** (2007) 052 and arXiv:0705.2983 [hep-ph]; R. M. Godbole, D. J. Miller, 2 and M. M. Muhlleitner, JHEP **0712**, 031 (2007); C. Ruwiedel, N. Wermes and M. Schumacher, Eur. Phys. J. C **51**, 385 (2007); S. Berge, W. Bernreuther and J. Ziethe, Phys. Rev. Lett. **100**, 171605 (2008); S. Berge and W. Bernreuther, Phys. Lett. B **671**, 470 (2009); S. Berge, W. Bernreuther, B. Niepelt, H. Spiesberger, [arXiv:1108.0670 [hep-ph]]; C. Englert, C. Hackstein and M. Spannowsky, Phys. Rev. D **82**, 114024 (2010); F. Campanario, M. Kubocz and D. Zeppenfeld, Phys. Rev. D **84**, 095025 (2011); C. Englert, M. Spannowsky and M. Takeuchi, JHEP **1206**, 108 (2012); D. Stolarski and R. Vega-Morales, arXiv:1208.4840 [hep-ph]. Y. Gao, A. V. Gritsan, Z. Guo, K. Mel-

- nikov, M. Schulze and N. V. Tran, Phys. Rev. D **81**, 075022 (2010); J. Ellis and D. S. Hwang, JHEP **1209**, 071 (2012); A. Alves, arXiv:1209.1037 [hep-ph]. S. Bolognesi, Y. Gao, A. V. Gritsan, K. Melnikov, M. Schulze, N. V. Tran and A. Whitbeck, arXiv:1208.4018 [hep-ph]; R. Boughezal, T. J. LeCompte and F. Petriello, arXiv:1208.4311 [hep-ph]; J. Ellis, D. S. Hwang, V. Sanz and T. You, arXiv:1208.6002 [hep-ph]; S. Y. Choi, M. M. Muhlleitner and P. M. Zerwas, arXiv:1209.5268 [hep-ph]; J. Kumar, A. Rajaraman and D. Yaylali, arXiv:1209.5432 [hep-ph]; C. -Q. Geng, D. Huang, Y. Tang and Y. -L. Wu, arXiv:1210.5103 [hep-ph]; J. Ellis, R. Fok, D. S. Hwang, V. Sanz and T. You, arXiv:1210.5229 [hep-ph]; A. Freitas and P. Schwaller, arXiv:1211.1980 [hep-ph]; J. Ellis, V. Sanz and T. You, arXiv:1211.3068 [hep-ph].
- [10] L. D. Landau, Dokl. Akad. Nauk., USSR **60**, 207 (1948); C. N. Yang, Phys. Rev. **77**, 242 (1950); for an alternative viewpoint, see J. P. Ralston, arXiv:1211.2288 [hep-ph].
- [11] K. Arnold, J. Bellm, G. Bozzi, F. Campanario, C. Englert, B. Feigl, J. Frank and T. Figy *et al.*, arXiv:1207.4975 [hep-ph]; K. Arnold, J. Bellm, G. Bozzi, M. Brieg, F. Campanario, C. Englert, B. Feigl, J. Frank *et al.*, [arXiv:1107.4038 [hep-ph]]; K. Arnold, M. Bahr, G. Bozzi, F. Campanario, C. Englert, T. Figy, N. Greiner and C. Hackstein *et al.*, Comput. Phys. Commun. **180** (2009) 1661.
- [12] C. Englert, B. Jager, D. Zeppenfeld, JHEP **0903** (2009) 060.
- [13] M. Fierz, Helv. Phys. Acta **12**, 3 (1939); M. Fierz and W. Pauli, Proc. Roy. Soc. Lond. A **173**, 211 (1939); H. van Dam and M. J. G. Veltman, Nucl. Phys. B **22**, 397 (1970).
- [14] K. Hagiwara, J. Kanzaki, Q. Li and K. Mawatari, Eur. Phys. J. C **56**, 435 (2008).
- [15] G. F. Giudice, R. Rattazzi and J. D. Wells, Nucl. Phys. B **544**, 3 (1999).
- [16] B. Jager, C. Oleari, D. Zeppenfeld, JHEP **0607** (2006) 015.
- [17] B. Jager, C. Oleari, D. Zeppenfeld, Phys. Rev. **D73** (2006) 113006.
- [18] G. Bozzi, B. Jager, C. Oleari, D. Zeppenfeld, Phys. Rev. **D75** (2007) 073004.
- [19] J. Frank, <http://www-itp.particle.uni-karlsruhe.de/diplomatheses.de.shtml>
- [20] H. Murayama and I. Watanabe and K. Hagiwara, KEK-91-11.
- [21] J. Alwall, P. Demin, S. de Visscher, R. Frederix, M. Herquet, F. Maltoni, T. Plehn, D. L. Rainwater *et al.*, JHEP **0709** (2007) 028.
- [22] T. Figy, C. Oleari, D. Zeppenfeld, Phys. Rev. **D68** (2003) 073005.
- [23] S. Catani, M. H. Seymour, Nucl. Phys. **B485** (1997) 291-419.
- [24] W. Siegel, Phys. Lett. B **84**, 193 (1979); W. Siegel, Phys. Lett. B **94**, 37 (1980).

- [25] A. Denner and S. Dittmaier, Nucl. Phys. B **734**, 62 (2006).
- [26] G. Passarino, M. J. Veltman, Nucl. Phys. **B160**, 151 (1979).
- [27] C. Oleari, D. Zeppenfeld, Phys. Rev. **D69** (2004) 093004.
- [28] A. Denner, S. Dittmaier, M. Roth, D. Wackeroth, Nucl. Phys. **B560** (1999) 33-65.
- [29] K. Nakamura et al. (Particle Data Group), J. Phys. G 37, 075021 (2010)
- [30] J. Pumplin, D. R. Stump, J. Huston, H. L. Lai, P. M. Nadolsky, W. K. Tung, JHEP **0207** (2002) 012.
- [31] H. -L. Lai, M. Guzzi, J. Huston, Z. Li, P. M. Nadolsky, J. Pumplin, C. -P. Yuan, Phys. Rev. **D82** (2010) 074024.
- [32] M. H. Seymour, Nucl. Phys. **B513** (1998) 269-300.
- [33] S. Frixione, Phys. Lett. **B429** (1998) 369-374.
- [34] A. Heister, O. Kodolova, V. Konoplyanikov, S. Petrushanko, J. Rohlf, C. Tully, A. Ulyanov, CERN-CMS-NOTE-2006-036
- [35] T. Figy and D. Zeppenfeld, Phys. Lett. B **591** (2004) 297.
- [36] K. Hagiwara, Q. Li and K. Mawatari, JHEP **0907**, 101 (2009).
- [37] C. Englert, B. Jager, M. Worek and D. Zeppenfeld, Phys. Rev. D **80** (2009) 035027.